Nanoscopic dopamine transporter distribution and conformation are inversely regulated by excitatory drive and D_2-autoreceptor activity

Matthew D. Lycas[1], Aske L. Ejdrup[1], Andreas T. Sørensen[1], Nicolai O. Haahr[1], Søren H. Jørgensen[1], Daryl A. Guthrie [2], Jonatan F. Støier[1], Christian Werner[3], Amy Hauck Newman[2], Markus Sauer[3], Freja Herborg[1] and Ulrik Gether[1, 4,*]

[1]Molecular Neuropharmacology and Genetics Laboratory, Department of Neuroscience, Faculty of Health and Medical Sciences, Maersk Tower 7.5, University of Copenhagen, DK-2200 Copenhagen, Denmark

[2]Medicinal Chemistry Section, Molecular Targets and Medications Discovery Branch, National Institute on Drug Abuse-Intramural Research Program, National Institutes of Health, Baltimore, Maryland 21224

[3]Department of Biotechnology and Biophysics, Biocenter, Julius-Maximilians-Universität Würzburg, Am Hubland, 97074 Würzburg, Germany

[4]Lead contact

*Correspondence: gether@sund.ku.dk

SUMMARY

The nanoscopic organization and regulation of individual molecular components in presynaptic varicosities of neurons releasing modulatory volume neurotransmitters like dopamine (DA) remain largely elusive. Here we show by application of several super-resolution microscopy techniques to cultured neurons and mouse striatal slices, that the dopamine transporter (DAT), a key protein in varicosities of dopaminergic neurons, exists in the membrane in dynamic equilibrium between an inward-facing nanodomain-localized and outward-facing unclustered configuration. The balance between these configurations is inversely regulated by excitatory drive and by DA D2-autoreceptor activation in manner dependent on Ca^{2+}-influx via N-type voltage-gated Ca^{2+}-channels. The DAT nanodomains contain tens of transporters molecules and overlap with nanodomains of PIP2 (phosphatidylinositol-4,5-bisphosphate) but show little overlap with D2-autoreceptor, syntaxin-1 and clathrin nanodomains. Summarized, the data reveal a mechanism for rapid alterations in nanoscopic DAT distribution and show a striking link of this to the conformational state of the transporter.

Keywords: super-resolution microscopy; dSTORM; PALM, expansion microscopy; neurotransmitter transporters; dopamine transporter; dopamine receptors; PIP2; fluorescent cocaine analogues; volume transmission; synaptic architecture; nanodomains

INTRODUCTION

In its 15 years of utilization, super-resolution microscopy has improved our insights into the molecular organization and dynamic regulation of pre- and postsynaptic structures in the brain. Indeed, it has become clear that regulatory processes of fundamental importance for spatial and temporal control of synaptic signaling occur at a nanoscale level. In excitatory synapses, for example, it is now believed that AMPA-type and NMDA-type ionotropic glutamate receptors segregate into distinct nanodomains in the postsynaptic density and that this co-organization plays a critical role in synaptic physiology (Choquet and Hosy, 2020; Groc and Choquet, 2020). Such studies highlight the importance of observing past the diffraction limit of visible light while still leveraging labeling strategies and live imaging compatibility that light microscopy provides (Choquet and Hosy, 2020; Groc and Choquet, 2020; Liu and Kaeser, 2019).

Much less is known about the nanoscale architecture of the presynaptic compartment in neurons releasing modulatory transmitters like dopamine (DA). DA neurons project from the midbrain to the basal ganglia, the limbic system and the prefrontal cortex to mediate the role of DA in motor functions, reward mechanisms and learning processes (Bjorklund and Dunnett, 2007; Iversen, 1975; Tritsch and Sabatini, 2012). The DA neurons have remarkable axonal arbors with numerous release sites (i.e. varicosities) (Descarries et al., 1996; Giguere et al., 2019), and DA neurotransmission differs from classical fast synaptic transmission by operating perhaps primarily via “volume transmission”; that is, DA is predominantly released from non-synaptic release sites to act on target cells often located micrometers away (Borroto-Escuela et al., 2018; Descarries *et al.*, 1996). It remains nonetheless elusive how the different molecular components in the dopaminergic release sites need to be organized at a nanoscale level and individually regulated to enable proper neurotransmitter release and reuptake.

A key regulator of DA neurotransmission, the dopamine transporter (DAT), is highly expressed in the varicosities of DA neurons and removes released DA from the extracellular space. DAT has received attention as the primary target for therapeutics, such as methylphenidate, and drugs of abuse such as

47 methamphetamine and cocaine (German et al., 2015; Kristensen et al., 2011; Torres and Amara, 2007).
48 Not surprisingly, DAT is subject to tight regulation through several mechanisms involving post-
49 translational modifications, protein-protein interactions and protein-lipid interactions (Bermingham and
50 Blakely, 2016; Eriksen et al., 2010; German *et al.*, 2015; Kristensen *et al.*, 2011; Ramamoorthy et al., 2011;
51 Torres, 2006). Moreover, we recently showed by application of super-resolution imaging that DAT
52 regulation might involve mechanisms that cannot be revealed by more classical methods (Rahbek-
53 Clemmensen et al., 2017). Our data showed that DAT localizes to discrete nanodomains in the plasma
54 membrane of cultured DA neurons and that activation of NMDA-receptors reduced DAT nanodomain
55 localization (Rahbek-Clemmensen *et al.*, 2017). Although this indicated that nanoscale dynamics in
56 dopamine varicosities could be critical for controlling DA neurotransmission, the mechanisms and
57 functional implications remain unknown.

58 Here we use several super-resolution imaging techniques, including Photoactivated Localization
59 Microscopy (PALM) (Betzig et al., 2006), direct Stochastic Optical Reconstruction Microscopy (dSTORM)
60 (Heilemann et al., 2008; Huang et al., 2009), 10 x Expansion Microscopy (ExM) (Chen et al., 2015; Tillberg
61 et al., 2016; Truckenbrodt et al., 2019) and single-particle tracking dSTORM (spt-dSTORM) (Manley et al.,
62 2008) together with new fluorescent cocaine-analogues (Guthrie et al., 2020) and new data analysis tools,
63 to investigate how DAT and associated molecular components at DA varicosities are dynamically
64 regulated. In summary, our experimental efforts demonstrate that excitatory drive and D2-autoreceptor
65 activity inversely regulate in a Ca^{2+} dependent manner the conformational state of DAT and its localization
66 in DA varicosities to PIP2 enriched nanodomains separate from syntaxin-1 (STX-1), D2-autoreceptor or
67 clathrin nanodomains. In this way, our study uncovers a hitherto unknown level of regulation of an
68 essential membrane protein in a modulatory transmitter terminal.

69

70

71 **RESULTS**

72 **DAT shows nanodomain distribution in cultured neurons and striatal slices**

73 There are a variety of strategies to resolve biological structures past the diffraction limit of light, but each
74 method is associated with strengths, compromises, and potential artefacts. True nanoscopic
75 organizational principles should therefore be observed across a variety of super-resolution methods as
76 well as model systems. Our previous dSTORM work suggested that DAT distributes into nanodomains at
77 DA varicosities of cultured midbrain DA neurons (Rahbek-Clemmensen *et al.*, 2017). To substantiate this
78 finding, we decided to assess DAT distribution across a variety of super-resolution methods and ultimately
79 investigate whether DAT is distributed into nanodomains in intact tissue. First, by magneto-transfection
80 we expressed in the DA neurons DAT with the photoconvertible fluorescent protein mEOS2 (Baker et al.,
81 2010) fused to the N-terminus. This enabled us to visualize distribution of the transporter without use of
82 antibodies. Importantly, images of tyrosine hydroxylase (TH) positive varicosities revealed a clustered
83 distribution of the mEOS2-DAT signal surrounding the cytosolic TH signal (Figure 1A-D), similar to that
84 seen by imaging the endogenous DAT by dSTORM (Rahbek-Clemmensen *et al.*, 2017). We next employed
85 astigmatic 3D-dSTORM to show that the DAT nanodomains were localized to the periphery of the
86 varicosities, substantiating that DAT is found mainly in the plasma membrane (Figure 1E-H). To assess the
87 distribution of DAT in intact tissue, we analyzed coronal mouse brain slices (Figure 1I-L). Widefield imaging
88 exposed the DAT positive varicosities and by dSTORM we could visualize DAT in single varicosities,
89 showing a nanodomain distribution like that seen in cultured neurons (Figure 1I-L). To exclude that the
90 observed distribution of DAT was not caused by artifacts introduced by the single molecule localization
91 microscopy approach (e.g., "overcounting" (Shivanandan et al., 2014)), we turned to ExM where
92 nanoscale spatial resolution is obtained by expanding the tissue sample using a polymer system (Chen *et*
93 *al.*, 2015). We employed a 10x expansion protocol (Truckenbrodt *et al.*, 2019) to mouse striatal slices
94 before imaging DAT in the slices by use of a spinning disk confocal microscope (Figure 1M-P). In the

95 stained expanded sample, we captured the intermingled axonal network of DA neurons while at the same
96 time observing clustering of DAT into nanodomains in varicosities (Figure 1M-P). Summarized, the
97 distribution of DAT into nanodomains in the plasma membrane of DA neurons was substantiated by
98 several high-resolution imaging techniques.

99 Having reaffirmed the clustered organization of DAT with different techniques and in intact brain
100 tissue, we decided to focus on the dSTORM technology in our subsequent studies because of its
101 quantitative nature and single-molecule sensitivity. To derive quantitative measures for the clustered
102 distribution of DAT, we employed the DBSCAN algorithm (density based spatial clustering of applications
103 with noise) (Ester et al., 1996; Rahbek-Clemmensen *et al.*, 2017) and extracted two key parameters from
104 the analysis: the size of the nanoclusters and the density of localizations within the clusters (Fig. 1Q-S).
105 The size was quantified as the fraction of clusters with a diameter >75 nm (Figure 1R). This size was chosen
106 as threshold to exclude any clusters that might be the result of amplified labeling of single proteins and
107 thus might arise from the antibody labeling methodology. By assessing the density of localizations as well,
108 we could determine changes in the number of molecules in a cluster without a change in cluster size.
109 Dense clusters were defined as clusters with >80 localizations within a radius of 50 nm (dense clusters in
110 red) (Figure 1S). In selected cases, we also employed Voronoi tessellation to compare the density
111 distributions of localization following pharmacological treatments in a parameter free fashion (Levet et
112 al., 2019). In this use of Voronoi tessellation, clusters themselves were not identified but localization
113 density changes could be detected with greater sensitivity (Figure 1T).

114 To estimate how many DAT molecules that are present in an average DAT nanodomain defined by
115 the DBSCAN analysis, we used a protocol modified from (Ehmann et al., 2014; Siddig et al., 2020) and
116 labeled cultured DA neurons with sequential dilutions of the primary DAT antibody. This enabled us to
117 define that a minimum cluster is made from ~three localizations and that an average large cluster contains
118 ~33 copies of the antibody corresponding to 50-100 DAT molecules as a rough estimate (Figure S1). The

119 same data series lent itself perfectly for cluster analysis by varied label density cluster verification,
120 enabling us to distinguish between random clustering arising from multiple observations of single
121 fluorophores and true clustering (Baumgart et al., 2016). In agreement with our data in DAT expressing
122 Cath.a-differentiated (CAD) cells (Rahbek-Clemmensen *et al.*, 2017), our analysis supported that the
123 clustering behavior of DAT in cultured neurons reflect true nanocluster formation (Figure S2).
124

125 **Nanodomain localized DAT is preferentially in an inward-facing conformation**

126 To assess putative functional implications of the nanoclustered distribution of DAT, we investigated
127 whether this could involve a conformational bias with nanoclustered DAT having a different conformation
128 than unclustered DAT. Cocaine and cocaine-like inhibitors are known to bind with higher affinity to DAT
129 in the outward-facing conformation than in the inward-facing conformation (Beuming et al., 2008; Loland
130 et al., 2008; Newman et al., 2019). We envisioned accordingly (and in line with (Lebowitz et al., 2019))
131 that an indirect measure of the conformational state of DAT inside and outside the nanodomains could
132 be obtained by parallel imaging of binding to DAT of a fluorescently tagged cocaine-analogue and of DAT
133 itself; that is, as a result of its conformational bias the cocaine-analogue would be expected to bind more
134 to outward-facing than to inward-facing transporters at a subsaturating concentration. We labeled
135 cultured DA neurons and mEOS2-DAT expressing CAD cells with DG3-63 (10 nM), an analogue of cocaine
136 tagged with JF_{646} suited for dSTORM (Figure 2A-D). The DG3-63 signal generally appeared somewhat less
137 clustered as compared to that observed by our other approaches (see Figure 1). This might indicate a
138 preferential binding of DG3-63 to unclustered DAT, which was supported by dual-color images of DG3-63
139 labelled DAT and mEOS-DAT, showing a more dispersed DG3-63 signal as compared to a more clustered
140 mEOS2-DAT signal (Figure 2E-G). Importantly, the DG3-63 signal was specific as it was essentially
141 eliminated by excess of unlabeled cocaine (Figure 2H). To quantify whether DG3-63 preferentially bound
142 to unclustered DAT, we used a modification of the principles outlined by the colocalization extension of

143 the Voronoi tessellation algorithm (Levet *et al.*, 2019) where associated DG3-63 was identified by
144 including DG3-63 localizations within 25 nm from an mEOS2-DAT localization (Figure 2I-K). The total
145 mEOS2-DAT Voronoi tessellated area distribution showed a preference for smaller tessellated areas
146 consistent with a clustered distribution (Figure 2L). In contrast, the mEOS2-DAT-associated DG3-63
147 localizations resided on larger Voronoi tessellated areas; hence, DG3-63 binding was not enriched in the
148 DAT nanodomains containing the highest density of DAT molecules (Figure 2L). This suggests that
149 nanoclustered DAT are less prone to bind DG3-63, consistent with a more inward-facing transporter
150 conformation or a less accessible binding site. Interestingly, by analyzing the distribution of mEOS2-DAT
151 after treatment with an excess, and thereby saturating concentration, of cocaine, we observed a dispersal
152 of the signal. This supports that forcing the transporter into an outward-facing conformation may release
153 the transporter from the nanodomains (Figure S3A).

154 To further address this question, we examined the effect of the DAT inhibitors nomifensine,
155 JHW007 and ibogaine on DAT nanoclustering in CAD cells transiently expressing WT DAT. We decided to
156 use dSTORM and thus immunolabeling rather than mEOS2-DAT to make the data more compatible with
157 our analyses on neurons and brain slices. Of the different inhibitors, nomifensine is a cocaine-like inhibitor
158 prone to self-administration (Spyraki and Fibiger, 1981) a and thus prone to stabilize an outward-facing
159 conformation (Beuming *et al.*, 2008; Loland *et al.*, 2008; Newman *et al.*, 2019). JHW007 and ibogaine,
160 however, are known to promote an inward-facing conformation of the transporter (Beuming *et al.*, 2008;
161 Kasture et al., 2016; Loland *et al.*, 2008; Newman *et al.*, 2019). Importantly, a Voronoi tessellation analysis
162 of the data showed that while nomifensine decreased nanoclustering, both JHW007 and ibogaine
163 increased DAT clustering, consistent with the notion that an inward-facing conformation promotes
164 nanodomain localization (Figure S3B, C).

165 We further rationalized that if the nanoscale DAT distribution reflects its molecular conformation,
166 then a redistribution would be expected for a DAT variant with a conformational bias. Accordingly, we

167 compared in transfected CAD cells clustering of WT DAT with that of a disease-associated DAT mutation
168 (D421N) known to be shifted towards an inward-facing conformation (Hansen et al., 2014; Herborg et al.,
169 2018) (Figure 2M-R). In agreement with the idea that inward-facing DAT will display preferential
170 localization to nanodomains, analysis of the resulting dSTORM data revealed for D421N compared to WT
171 both a higher fraction of large clusters (diameter >75 nm) and a higher fraction of localizations in dense
172 clusters (Figure 2N, O, Q, R) without a change in total number of detected localizations (Fig. 2P).
173 Summarized, the data support that DAT preferentially assumes an inward-facing conformation in DAT
174 nanodomains while the conformation outside the nanodomains conceivably is more outward-facing.
175
176 **NMDA receptor activation declusters DAT in striatal slices**
177 We next assessed whether DAT nanodomain distribution was sensitive to NMDA stimulation in intact
178 tissue (Figure 2I-P) as we previously observed in cultured neurons (Rahbek-Clemmensen *et al.*, 2017).
179 Notably, NMDA receptors are present in DA terminals where they can stimulate DA release (Salamone et
180 al., 2014). Acute coronal striatal slices were treated for 5 min with vehicle, NMDA or NMDA plus the
181 NMDA receptor antagonist (2R)-amino-5-phosphonovaleric acid (AP5) before DAT immunolabeling and
182 dSTORM (Figure 3A). Because each dSTORM image contained a vast number of DAT positive varicosities,
183 we developed a new collection algorithm for automated and unbiased isolation of these varicosities,
184 allowing subsequent quantification of DAT clustering (Figure 3B, C). Following NMDA treatment, both the
185 fraction of clusters >75 nm and the faction of localizations in dense clusters decreased; an effect that was
186 muted by the NMDA antagonist AP5 (Figure 3D, E). Note that the comparisons were normalized to the
187 control sample from the individual imaging session to correct for unavoidable variability in sample
188 preparations and between imaging sessions. Importantly, the data were further supported by Voronoi
189 tessellation showing that NMDA, but not NMDA + AP5, reduced the fraction of smaller tessellated areas

190 and thus clustering (Figure 3F). We conclude that local activation of NMDA receptors in intact tissue
191 promotes dispersal of DAT nanodomains.
192
193 **DAT nanodomain localization is regulated by neuronal activity**
194 We speculated whether persistent changes in membrane potential and thereby in neuronal excitability
195 would affect DAT nanodomain distribution. To test this, we expressed the bacterial sodium channel
196 (mNaChBac) or the inward-rectifier potassium channel (Kir2.1) (Lin et al., 2010; Xue et al., 2014) in
197 cultured DA neurons to make them more or less excitable, respectively (Lin *et al.*, 2010). As a control, we
198 also expressed an inactive mutant of mNaChBac (mNaChBac MUT) (Lin *et al.*, 2010; Xue *et al.*, 2014). In
199 agreement with selective expression in DA neurons, we confirmed that transduced cells were also DAT
200 positive (Figure S4). Electrophysiological recordings on single neurons showed that the pacemaker firing
201 activity of DA neurons (Rayport et al., 1992) was enhanced in mNaChBac-expressing neurons and reduced
202 in Kir2.1 expressing neurons with no significant change in mNaChBac MUT-expressing neurons (Fig S4).
203 Analysis by dSTORM of DAT distribution in mNaChBac expressing neurons showed decreased clustering,
204 while for Kir2.1 expressing neurons we saw a trend towards an increased fraction of large clusters and a
205 significant increase in localizations within large dense clusters (Fig. 4A-D). No significant effect was seen
206 for mNaChBac MUT (Figure 4C, D). Thus, DAT nanodomain localization is in cultured DA neurons regulated
207 by persistent changes in excitability or firing activity with increased activity leading to dispersal of DAT
208 from nanodomains and decreased activity leading to increased nanodomains localization.
209
210 **DAT nanodomain localization is regulated by Ca^{2+}**
211 Because of the effect of neuronal excitability, we decided to investigate putative involvement of Ca^{2+}
212 influx via voltage-gated Ca^{2+} channels (VGCC) in NMDA-induced DAT declustering. Note that both P/Q
213 type and N-type VGCCs should be present in DA terminals (Turner et al., 1993). DA neurons were

214 stimulated with NMDA for 5 min with or without the N-type VGCC blocker ω-conotoxin or the P/Q type
215 VGCC blocker ω-agatoxin. While we observed no effect of ω-agatoxin, the dispersing effect of NMDA on
216 DAT clustering was essentially abolished by ω-conotoxin. Similarly, Voronoi tessellation analysis showed
217 that ω-conotoxin, but not ω-agatoxin, blocked the NMDA-induced shift away from small, tessellated areas
218 and thus blocked the dispersal of DAT nanodomains (Figure 4E-J, Movies S1-2). We next asked whether
219 Ca^{2+} would be important *per se* by preincubating the neurons with the cell permeable Ca^{2+}-chelator
220 BAPTA-AM. Indeed, BAPTA-AM blunted the response to NMDA (Figure 4K-L). Of note, the
221 pharmacological data fitted well with available single-cell mRNA sequencing data on DA neurons
222 supporting highest transcription of N-type VGCC in DA neurons (Figure 4M) (see Methods for data bases
223 used). Taken together, NMDA-induced dispersal of DAT nanodomains appears to occur via Ca^{2+}-
224 dependent mechanism involving the activity of N-type VGCCs.
225
226 **DAT nanodomain localization is regulated by the D2 autoreceptor**
227 D2-autoreceptors in DA neurons act as negative feedback regulators decreasing neuronal excitability and
228 firing activity by promoting opening of inhibitory G-protein-activated inwardly rectifying potassium
229 channels (Beckstead et al., 2004; Kuzhikandathil et al., 1998). We surmised that D2-autoreceptor activity
230 might regulate localization of DAT to nanodomains and tested this by determining the effect of the D2
231 receptor antagonist haloperidol and the D2 receptor agonist quinpirole. Interestingly, incubation with 10
232 nM haloperidol for 5 min resulted in dispersal of DAT nanodomains with a reduced fraction of clusters
233 >75 m, fewer localizations in dense clusters and a reduced fraction of smaller Voronoi tessellated areas
234 (Figure 5A-F, Movies S1, S3). This effect is likely the result of haloperidol blocking the effect on the D2-
235 autoreceptors of DA released in the culture as a consequence of DA neuronal pacemaker activity as shown
236 in Figure S4. Also, co-incubation with an excess of quinpirole blocked the effect of haloperidol (Figure 5A-
237 F). Moreover, the effect of haloperidol was accompanied by an increase in cytoplasmic free Ca^{2+}

238 consistent with D2-autoreceptor activity suppressing neuronal firing (Figure S5A, B). This prompted us to
239 test if the effect of haloperidol, like the effect of NMDA, was dependent on Ca^{2+}- influx via N-type VGCCs.
240 This appeared to be the case as ω-conotoxin, but not ω-agatoxin, eliminated the effect of haloperidol
241 (Figure 5A-F). Summarized, our data support that D2-autoreceptors are preoccupied with DA in the
242 neuronal culture and that the activity of these receptors can regulate DAT nanodomain localization via a
243 Ca^{2+}-dependent mechanism.

244 To further substantiate a correlation between D2-autoreceptor signaling, neuronal activity and DAT
245 nanoclustering, we incubated cultured DA neurons with an antibody directed towards the luminal end of
246 the presynaptic vesicular protein, synaptotagmin-1. Upon exocytotic release, this luminal epitope is
247 exposed to the extracellular space and, thus, the degree of synaptotagmin-1 labeling can be considered
248 a proxy for exocytotic release activity (Truckenbrodt et al., 2018). Indeed, when blocking the D2
249 autoreceptor with haloperidol, this did not only cause dispersal of DAT nanoclusters but was also
250 accompanied by increased synaptotagmin-1 labeling as a likely result of increase exocytotic release
251 activity (Figure S5C). Importantly, it is unlikely that the presumed increase in exocytotic release of DA
252 directly regulates DAT and leads to dispersal of DAT nanodomains. Adding exogenous DA to the culture
253 had no effect on DAT nanoclustering (Figure S3D) and, moreover, DAT nanoclustering was unaffected by
254 noribogaine, while nomifensine caused a significant declustering of DAT (Figure S3D). This suggests that
255 the transporter already is preoccupied by DA and thereby is active/cycling, which expectably pushes a
256 fraction of the transporter molecules into an inward-facing nanoclustered configuration. In this scenario,
257 no effect is expected of noribogaine as well as it is consistent with the declustering seen in response to
258 nomifensine that will compete DA away from the transporter.

259

260 **Single particle tracking supports nanodomain dispersal in response to neuronal activity**

261 To obtain a better understanding of the dynamics underlying DAT nanodomain localization, we employed

262 SPT-dSTORM (Manley *et al.*, 2008) to assess if dispersal of DAT from nanodomains is accompanied by
263 increased lateral mobility of DAT in the membrane. To allow visualization in live cells, we labeled DAT in
264 DA neurons with a Janelia Fluor®549-conjugated cocaine analogue, DG3-80, suited for live dSTORM
265 (Guthrie *et al.*, 2020) (Figure 5G, H). Individual DAT tracks were captured with lengths up to 1.6 sec (100
266 frames, 16 msec frame rate) with the majority being 10-20 frames (Figure 5I, J). Separating tracks into
267 those reflecting confined movements and those reflecting freely moving particles showed that ~90% of
268 the tracks described freely moving particles (Figure 5K, L). Note that this distribution (with most of the
269 labeled molecules being freely moving) likely reflects preferential binding of DG3-80 to unclustered DAT
270 in the outward-facing conformation (Figure 2). The mean jump distance (i.e. the distance an individual
271 molecule/particle has traveled between each image) was ~110 nm for all the recorded tracks and ~50 nm
272 for static tracks only (Figure 5M, N). Interestingly, a jump distance of ~110 nm is so fast that a transporter
273 molecule might move 7-14 µm during a transport cycle estimated to last 1-2 sec (Prasad and Amara,
274 2001). Among the freely moving particles, there were even some that moved very fast with mean jump
275 distance of 200-350 nm (Figure 5M-O). Both NMDA receptor activation and blockade of the D2-
276 autoreceptors with either haloperidol or the neutral antagonist UH-232 increased the population of DAT
277 molecules with mean jump distances >200 nm, indicative of a possible link between dispersal of DAT
278 nanodomains and increased lateral mobility. Note that the similar effect of UH-232 and haloperidol
279 strongly suggest that their effect reflects blockade of D2-autoreceptors activated by DA, which is released
280 because of DA neuronal pacemaker activity, and not inhibition of constitutive receptor activity (Strange,
281 2008).
282
283 **DAT nanodomains overlap with PIP2 nanodomains**
284 A key question is how the nanoscale distribution of DAT relates to other molecular components of DA
285 terminals. We first turned to the plasma membrane phospholipid, PIP2, which can bind DAT and in doing

286 so modulate DAT activity (Belovich et al., 2019). Dual-color dSTORM on PIP2 and DAT in DA neurons
287 showed as expected (van den Bogaart et al., 2011), a distribution of the PIP2 signal into nanodomains
288 (Figure 6). Strikingly, these nanodomains showed a remarkable overlap with DAT nanodomains with the
289 Voronoi tessellation distributions revealing a large fraction of PIP2 localizations associated with dense
290 DAT localizations (Figure 6A, B, F). As also seen for DAT domains, treatment with both NMDA and
291 haloperidol reduced PIP2 localizations in large dense clusters while haloperidol also reduced cluster size.
292 Importantly, all these changes were blocked by AP5 or quinpirole, respectively (Figure 6B-D). The NMDA
293 and haloperidol-induced changes were reflected in the Voronoi tessellation distributions as well by
294 showing dispersal of the PIP2 nanodomains and reduced PIP2 association to nanoclustered DAT (Figure
295 6E, F).
296
297 **The D2R is also shows nanodomain distribution**
298 We next analyzed the D2-autoreceptors that are found both in the somatodendritic compartment of DA
299 neurons and in DA terminals. Due to known challenges with DA receptor antibodies, we both validated
300 the specificity of the antibody in transfected HEK293 cells and on slices from D2 receptor knock-out mice
301 (Figure S6). Subsequent dual-color dSTORM experiments on cultured DA neurons revealed a clustered
302 distribution of the D2-autoreceptors with nanodomains of a similar size as those found for DAT (Figure
303 7A, B). Furthermore, like our findings for DAT and PIP2, NMDA and haloperidol promoted dispersal of the
304 receptor domains (Figure 7B-E). Relatively few of the nanodomains, however, overlapped with the DAT
305 domains as apparent from the Voronoi tessellation distributions (Figure 7A, B, F), and as for D2-
306 autoreceptor association to DAT, we only observed marginal changes upon NMDA and haloperidol
307 treatment (Figure 7F).
308 The findings prompted us to further assess the specificity of the pharmacological manipulations by
309 imaging additional key membrane components in DA terminals including clathrin (Maxfield and McGraw,

310 2004) and the single transmembrane SNARE protein syntaxin1 (STX-1). Imaging of clathrin revealed a
311 nanoclustered distribution, possibly corresponding to clathrin-coated pits (Li et al., 2018), that showed
312 little co-localization with DAT and, importantly, essentially no change in distribution in response to NMDA
313 (Figure S7). We also recapitulated nanodomain distribution of STX-1 that is known to exist in such domains
314 in presynaptic terminals (Padmanabhan et al., 2020) as well as the protein has been proposed to bind
315 DAT (Binda et al., 2008). However, the STX-1 domains showed little overlap with DAT and responded
316 differently to NMDA with a decreased fraction of large clusters and an increased fraction of localizations
317 in dense clusters (Figure S7). Note, however, that NMDA slightly increased localization of STX1 to
318 unclustered DAT (i.e. the larger tessellated areas) according to the Voronoi tesselated distributions
319 (Figure S6). In summary, several plasma membrane components of DA terminals show a nanoclustered
320 distribution that, however, appears to be differentially regulated.
321

322 **DISCUSSION**

323 DA neurons have remarkable axonal arbors with numerous presynaptic terminals or varicosities that serve
324 as the principal architectural units responsible for release and reuptake of DA. Nonetheless, we still have
325 a surprisingly poor understanding of the molecular organization of these varicosities, and what regulatory
326 processes that might take place within these compartments that are less than ~1 µm in size. Indeed, most
327 of these varicosities are non-synaptic release sites and it remains unclear whether this results in less
328 stringent requirement of the spatial organization of the molecular machinery as compared to e.g.
329 glutamatergic synapses (Choquet and Hosy, 2020; Groc and Choquet, 2020; Liu and Kaeser, 2019). Here,
330 we utilize several super-resolution techniques to provide detailed, quantitative insights into how a key
331 membrane protein, DAT, is subject to nanoscale regulation within these varicosities. This regulation
332 involves Ca^{2+}-dependent movements of DAT in and out of PIP2-enriched nanodomains in the plasma
333 membrane, which are governed by NMDA receptor and D2-autoreceptor activity, and likely involves shift
334 of DAT between outward and inward-facing conformations.

335 To firmly substantiate that DAT is distributed into nanodomains in the plasma membrane of DA
336 neurons, we applied a range of different super-resolution microscopy techniques to both cultured
337 neurons and striatal slices. A varied label density cluster analysis (Baumgart *et al.*, 2016) supported that
338 our dSTORM procedure reports true nanodomains, which was further confirmed by ExM, excluding
339 potential artifacts from multiple countings of the same fluorophore. A rough estimate of the number of
340 DAT molecules suggested the presence of 50-100 DAT molecules within each domain, which is in the same
341 range estimated for AMPA receptor domains in the postsynapse (~25 molecules) (Goncalves et al., 2020).
342 Importantly, by using the novel fluorescent cocaine analogue DG3-63 and analyzing the effect of
343 conformationally biased ligands including noribogaine, JHW007 and nomifensine, we were able to obtain
344 evidence that DAT displays a conformational bias depending on whether it is present in a nanodomain or
345 not. This was further supported by analyzing the disease-associated DAT mutant D421N that displays

346 lowered DA affinity and is biased towards an inward-facing conformation. We should nonetheless note
347 that the distribution of D421N could be affected by the cation leak and anomalous DA efflux that
348 previously have been associated with this mutant (Herborg *et al.*, 2018). However, it is appealing to
349 envision that a distribution of DAT between a nanoclustered, inward-facing population of transporter
350 molecules and an unclustered, "free" outward-facing population of DAT molecules represents a means
351 by which DAT activity can be regulated on a very fast time scale. A possible question is whether this
352 dynamic localization of DAT to nanodomains involves changes in DAT oligomerization; however, we find
353 this unlikely considering recent data supporting the existence in the plasma membrane of DA dimers that
354 are highly stable even over the course of minutes (Das et al., 2019). Given the large fraction of DAT present
355 in nanodomains It is also unlikely that DAT in nanodomains just constitutes DAT preparing for
356 internalization. But DAT may internalize from the nanodomains as the inward-facing conformation
357 previously has been associated with DAT internalization (Sorkina et al., 2009), which suggests that at least
358 some internalization takes place from the DAT nanodomains.

359 Of major importance, we validated in striatal slices the dispersing effect of NMDA on DAT
360 nanodomains by employing a novel Voronoi tessellation-based collection algorithm. In addition to
361 support that our findings in cultured DA neurons can be translated to intact tissue, the algorithm offers
362 possibilities for future detailed, quantitative analyses of protein distribution in neuronal terminals in
363 intact brain tissue. Another important observation was that both acute excitatory input, i.e. activation of
364 NMDA receptors, and sustained alterations of neuronal excitability, as evidenced by expression of either
365 mNaChBac or Kir2.1 (Lin *et al.*, 2010; Xue *et al.*, 2014) in DA neurons, affect the nanoscale distribution of
366 DAT in presynaptic varicosities. We also observed a marked role of presynaptic D2R activity, further
367 suggesting that the nanoscopic distribution of a membrane protein, such as DAT, is continuously adapted
368 by several mechanisms to the immediate activity level of the neurons in which it is expressed. It may be
369 considered that the effects of the pharmacological manipulations on DAT clustering are quantitatively

370 modest. However, the effects are highly significant, as well as it should be considered that the numerous
371 varicosities included in each quantification may be very heterogenous and possibly differentially sensitive
372 to treatments. Such heterogeneity is directly supported by the finding that only a subset of DA terminals
373 appeared active at any given time (Pereira et al., 2016). Future efforts should further clarify this
374 interesting issue.

375 Our data revealed a striking co-localization of DAT and PIP2 nanodomains, as well as a dispersing
376 effect of NMDA and haloperidol treatment on both types of domains. We also found that the effect of
377 haloperidol and NMDA on DAT nanodomains not only required opening of VGCCs but also was contingent
378 on the presence Ca^{2+}. Interestingly, an increase in cytosolic Ca^{2+} was previously shown to release
379 membrane protein sequestered PIP2, which might indicate a possible PIP2-dependent Ca^{2+}-regulation of
380 DAT nanodomain localization (McLaughlin and Murray, 2005). Indeed, the anionic lipid is known to form
381 nanodomains that have been suggested to be important for membrane protein nanoclustering, including
382 STX-1 (van den Bogaart *et al.*, 2011). Also, PIP2 is known to regulate many cellular processes including ion
383 channel and transporter function (Hamilton et al., 2014; Suh and Hille, 2008). Both the serotonin
384 transporter (SERT) and DAT bind PIP2 (Buchmayer et al., 2013; Hamilton *et al.*, 2014), and for DAT it was
385 suggested that PIP2 binds to the DAT N-terminus and induces a structural change that encourages
386 phosphorylation and a reverse transport mode of DAT critical for amphetamine-induced DA efflux
387 (Belovich *et al.*, 2019; Hamilton *et al.*, 2014). This is interesting in relation to our data that support an
388 inward-facing configuration of nanodomain localized DAT and thereby presumably a more efflux prone
389 transporter (Robertson et al., 2009). Of note, our previous study suggested a dependency on cholesterol
390 for DAT nanodomain distribution (Rahbek-Clemmensen *et al.*, 2017). Furthermore, previous data have
391 indicated that cholesterol binds to DAT and regulates its function by promoting an outward-facing
392 conformation (Hong and Amara, 2010). A conceivable explanation is that cholesterol serves to
393 compartmentalize the membrane to enable a nanoclustered co-distribution of DAT and PIP2 (Carquin et

394 al., 2016; Hwang et al., 1995), and accordingly that cholesterol rather interacts with unclustered, outward-
395 facing DAT. It is even possible that rapid movements of DAT in and out of nanodomains parallels the
396 transport cycle shifting the transporter back and forth from an outward-facing, substrate binding,
397 conformation and unclustered distribution to an inward-facing, substrate releasing (or efflux prone),
398 conformation and clustered distribution. Indeed, our single particle tracking data (Spt-STORM) show that
399 the mean jump distance for a given particle is r~110 nm in a 16 ms time frame (Figure 5M), suggesting
400 that a single DAT molecule moves 7-14 µm during a single transport cycle of 1-2 sec (Prasad and Amara,
401 2001). Thus, the movements in the membrane are fast enough for DAT molecules to move in and out of
402 nanodomains during a single transport cycle. Fast movements of DAT have also been supported with
403 classical single particle tracking techniques (Guthrie *et al.*, 2020) although use of large quantum dots for
404 labeling suggested somewhat slower diffusion speeds (Thal et al., 2019).

405 Previous data have indicated that stimulation of D2-autoreceptors of both the D2 and D3 subtype
406 enhance DAT activity (Bolan et al., 2007; Castro-Hernandez et al., 2015; Lee et al., 2007; Meiergerd et al.,
407 1993; Parsons et al., 1993; Zapata et al., 2007). Here we provide evidence that in the DA neuronal cultures
408 the D2-autoreceptor is preoccupied with DA and that this promotes DAT nanoclustering may be
409 consistent with such an enhancement; that is, if D2-autoreceptor activation causes an increase in DAT
410 activity, this would expectably lead to a shift of the DAT conformational equilibrium towards a more
411 inward-facing conformation and, hence, a likely shift towards a higher degree of nanodomain localization.
412 However, our data may challenge that the regulation of DAT by D2-autoreceptors involves a direct
413 interaction as previously suggested (Bolan *et al.*, 2007; Castro-Hernandez *et al.*, 2015; Lee *et al.*, 2007).
414 Although the D2-autoreceptor, like DAT, according to our dSTORM analyses, are distributed into
415 nanodomains, we observed only modest co-localization between the two proteins in the DA terminals.
416 The nanodomains responded, nonetheless, like DAT to NMDA and haloperidol, suggesting that excitatory
417 input promotes nanodomain dispersal, while D2 autoreceptor activation promotes nanoclustering. We

418 speculate that this increased clustering upon activation reflects assembly of the receptor with
419 intracellular signaling complexes and/or dynamics relating to desensitization and/or internalization.

420 DAT nanodomains showed rather little co-localization with nanodomains of STX-1 and clathrin that
421 importantly also responded differently to NMDA. These differential effects support that the changes we
422 see for DAT, the D2-autoreceptor and PIP2 most likely reflect true molecular redistributions and unlikely
423 are the result of non-specific changes. The decrease in STX-1 nanocluster size and increased localization
424 within dense clusters in response to NMDA is consistent with other studies indicating that breakup of STX-
425 1 nanodomains, correlating with vesicle release, takes place, while at the same time more STX-1 is being
426 brought to the sites of release (Maidorn et al., 2019; Padmanabhan *et al.*, 2020). Of interest, the Voronoi
427 tesselated distributions showed that NMDA slightly increased localization of STX1 to unclustered DAT (i.e.
428 the larger tessellated areas). This suggests that the previously described direct interaction between DAT
429 and STX-1, which have been proposed to be important for amphetamine-induced efflux (Binda *et al.*,
430 2008), may take place between the unclustered fractions of the two proteins.

431 Summarized, by application of single-molecule sensitive super-resolution imaging we show
432 compelling evidence that the molecular machinery supporting volume transmission mediated by a
433 neuromodulator like DA is subject to spatial and temporal nanoscale regulation with putative major
434 impact on synaptic function. The conclusion is substantiated by detailed studies of DAT that according to
435 our results is subject to remarkable nanoscale regulatory processes governed by excitatory input,
436 membrane potential, Ca^{2+} and activity of the presynaptic D2 receptor. Taken together, the present results
437 not only constitute a new framework for further deciphering the nanoscale architecture of presynaptic
438 release sites and the underlying functional implications for the DA system but also add to the growing
439 acknowledgment of nanoscopic regulation as a still poorly explored area of fundamental importance for
440 neuronal signaling.

441

442 **ACKNOWLEDGEMENT**

443 We thank Ralph Götz for support with expansion microscopy and Dr. Emiliana Borrelli for providing tissue
444 from D2R knock-out mice. The work was supported by the Lundbeck Foundation grants R266-2017-4331
445 (UG), R276-2018-792 (UG), R230-2016-3154 (M.D.L.), R181-2014-3090 (FH), R303-2018-3540 (F.H.) and
446 R231-2016-2481-5 (ATS), Independent Research Fund Denmark – Medical Sciences (U.G. 7016-00325B),
447 and the NIDA-Intramural Research Program Z1A DA000610 (AHN and DAG).

448

449 **AUTHOR CONTRIBUTIONS**

450 M.D.L. performed all the experiments and wrote the analyses not hereafter mentioned; A.L.E. devised
451 the cluster size algorithm, identified mRNA expression data and performed D2 receptor histology; A.T.S.
452 performed electrophysiology and generated the construct encoding Cre recombinase under control of a
453 truncated TH promotor; N.O.H. performed the D421N CAD cell experiments; S.H.J. cloned Kir2.1 and
454 mNaChBac plasmids and made non-commercially available viruses; D.A.G. and A.H.N. invented and
455 synthesized the fluorescent cocaine analogs; J.F.S. optimized the DA neuron culture protocol; M.D.L., F.H.,
456 and U.G. conceptualized the study, designed the research and interpreted data; U.G., F.H., M.S., and C.W.
457 supervised the research. M.D.L., U.G., and F.H. wrote the paper with contributions from M.S. and all the
458 other authors.

459

460 **COMPETING FINANCIAL INTERESTS**

461 The authors declare no competing interests.

462

463 **LEGENDS TO MAIN FIGURES**

464 **Figure 1. DAT shows nanodomain distribution in cultured neurons and striatal slices**

465 (A-D) Visualization of mEOS2-DAT overexpressed in cultured DA neurons. Endogenous TH was labeled to
466 identify DA neurons. (A, C) Widefield images (C is boxed region in A). (B, D) PALM/dSTORM images
467 (D is boxed region in B).

468 (E-H) 3D dSTORM image of DAT in DA neurons (color-coded based on depth). (E) Neuronal extension. (F)
469 Varicosity (boxed region in E) (XY perspective). (G) YZ perspective. (H) XZ perspective.

470 (I-L) Mouse brain coronal section immunolabeled for DAT. (I) brain slice with striatal DAT staining. (J)
471 Comparison of widefield with dSTORM. (K) Widefield view of varicosity. (L) dSTORM image.

472 (M-P) 10 x Expansion Microscopy (ExM) on mouse striatal slice immunolabeled for DAT. N shows region
473 of interest (R.O.I.) in M with the full 19 µM Z slice (color-coded based on depth); O is R.O.I. in M
474 with just 2 µM of the Z axis. (P) Single varicosity identified in O.

475 (Q-T) Cluster metrics demonstrated on a varicosity immunolabeled for DAT. Q, dSTORM of single
476 varicosity. (R, S) Identification of clusters by DBSCAN; clusters with diameter >75 nm in green,
477 clusters <75 nm in magenta; dense clusters (>80 localizations within a radius of 50 nm) in red. (T)
478 DAT localizations segmented by Voronoi tessellation.

479 See also Figures S1 and S2.

480

481 **Figure 2. Nanodomain localized DAT is preferentially in an inward-facing conformation**

482 (A-D) dSTORM on DA neurons and DAT expressing CAD cells labeled with the fluorescent cocaine
483 analogue DG3-63 (10 nM). (A) Axonal extension. (B) varicosity (box in A). (C) CAD cell. (D) R.O.I.
484 from C.

485 (E-H) The density-based association of DG3-63 to mEOS2-DAT. (E) Cartoon of labeling strategy. (F)
486 dSTORM/PALM image of CAD cell expressing mEOS2-DAT (red) and labeled with DG3-63 (10

487 nM)(blue). (G) Close-up dSTORM/PALM image of CAD cell expressing mEOS2-DAT (red) and labeled
488 with DG3-63 (10 nM) (blue). (H) The DG3-63 signal is blocked by 100 µM cocaine.
489 (I-K) Voronoi tessellation based colocalization algorithm. Tessellation is performed on the mEOS2-DAT
490 data and areas are marked for when the mEOS2-DAT localization has a DG3-63 localization within
491 25 nm distance.
492 (L) Left, Total mEOS2-DAT Voronoi tesselated area distribution (red) (probability density function
493 (P.D.F.) and tessellated areas of mEOS2-DAT associated with DG3-63 (blue). Right, tessellated areas
494 for mEOS2-DAT associated with DG3-63 (blue) compared to that associated in presence of
495 saturating cocaine.
496 (M-O) TIRF/dSTORM of WT DAT and inward-facing mutant (D421N). (M) Example image of DAT expressed
497 in CAD cells. (N) Example images of clusters with diameter >75 nm (green) in WT DAT and D421N
498 Dcells. (O) Normalized fraction of clusters with diameter >75 nm (in %), means ± S.E., from 38 WT
499 DAT cells and 42 D421N cells, 3 transfections, ***p<0.001, unpaired t-test.
500 (P-O) dSTORM of WT DAT and inward-facing mutant (D421N). (P) Number of localizations per μm^2 for
501 WT DAT and D421N, means ± S.E., unpaired t test, p= 0.4. (Q) Example image of dense clusters (red)
502 of WT DAT and D421N (radius 100 nm, >100 localizations). (R) Fraction of localizations in dense
503 clusters (in % of WT DAT), means ± S.E., from 38 WT DAT cells and 42 D421N cells, 3 transfections,
504 **p<0.01, unpaired t-test.
505 See also Figure S3.
506
507 **Figure 3. NMDA receptor activation declusters DAT in mouse brain slices**
508 (A) Workflow diagram.
509 (B) Data processing steps to isolate single varicosities from dSTORM images (see Methods).
510 (C) Representative DAT dSTORM image before, during, and after varicosity identification.

511 (D) Example varicosity from control, NMDA, and AP5 + NMDA treated slices (clusters with diameter
512 >75 nm in green, clusters <75 nm in magenta). Right, Normalized fraction of DAT clusters >75 nm
513 (in %), means ± S.E., from 3 experiments with analysis of 1793 control, 1102 NMDA and 1033 NMDA
514 + AP5 varicosities; one-way ANOVA, ****p<0.0001, *p<0.05.
515 (E) Example varicosity from control, NMDA (20 µM), and AP5 + NMDA (20 µM) treated slices (dense
516 clusters in red, >80 localizations, radius 50 nm). Right, Normalized fraction of DAT localizations in
517 dense clusters (in %), means ± S.E.; one-way ANOVA, ****p<0.0001, ***p<0.001, **p<0.01.
518 (F) The probability density functions (P.D.F.) for the Voronoi tessellated areas averaged by varicosity.
519
520 **Figure 4. DAT nanodomain localization is regulated by neuronal activity in a Ca^{2+} dependent manner**
521 (A-D) Expression of the Na^+ channel mNaChBac or the K^+ channel Kir2.1 in DA neurons. Example
522 varicosities from DAT dSTORM of control, mNaChBac or Kir2.1 expressing DA neurons. (A) DAT
523 clusters with diameter >75 nm in green, clusters <75 nm in magenta. (B) Dense DAT clusters in red
524 (>80 localizations, radius 50 nm). (C) Normalized fraction of clusters >75 nm (in %). (D) Normalized
525 fraction of DAT localizations in dense clusters (in %), means ± S.E.; data from 3 cultures and 128
526 control, 290 mNaChBac ,220 Kir2.1, and 211 mNaChBacMUT varicosities; one-way ANOVA,
527 ****p<0.0001, **p<0.01, *p<0.05, n.s., not significant.
528 (E-J) The effect of NMDA on DAT nanodomains is blocked by the N-type VGCC blocker ω-conotoxin.
529 Example varicosities from dSTORM of DA neurons subject to 5 min treatment with vehicle, NMDA
530 (20 µM), AP5 (100 µM) + NMDA (20 µM), ω-Conotoxin (1 µM) + NMDA (20 µM) or ω-Agatoxin (1
531 µM) + NMDA (20 µM). (E) DAT clusters with diameter >75 nm in green, clusters <75 nm in magenta.
532 (F) Dense DAT clusters in red (>80 localizations, radius 50 nm). (G) localizations segmented by
533 Voronoi tessellation. (H, I) Normalized fraction of DAT clusters >75 nm (in %) (H) and normalized
534 fraction of DAT localizations in dense clusters (in %) (I), means ± S.E.; one-way ANOVA, ****p<

535 <0.0001, *p<0.05, n.s., not significant. (J) Probability density functions (P.D.F.) (curves color-coded
536 as in the bar diagrams) for the Voronoi tessellated areas averaged by varicosity. Data are from 3
537 cultures and 190 control, 147 NMDA, 170 AP5, 180 ω-Conotoxin and 154 ω-Agatoxin varicosities,
538 (K, L) Pretreatment (30 in) with BAPTA-AM inhibits the dispersing effect of NMDA on DAT nanodomains.
539 (K) Normalized fraction of DAT clusters >75 nm (in %) and (L) normalized fraction of DAT
540 localizations in dense clusters (in %) for control, NMDA (20 µM) and NMDA (20 µM) + BAPTA-AM
541 (25 µM), means ± S.E.; data from 3 cultures and includes analysis of 66 control, 72 NMDA and 70
542 BAPTA-AM + NMDA varicosities, one-way ANOVA, **p<0.01, *p<0.05, n.s., not significant.
543 (M) mRNA expression for P, R, and N-type VGCC in DA neurons based on single cell RNAseq data (see
544 Methods).
545 See also Figure S4 and Movies S1-2.
546
547 **Figure 5. DAT nanodomain localization is regulated by the D2R and involves changes in lateral mobility**
548 A-F) Dispersal of DAT nanodomains is promoted by the D2R antagonist haloperidol and blocked by the
549 agonist quinpirole and by the N-type VGCC blocker ω-conotoxin. Example varicosities from
550 dSTORM of DA neurons subject 5 min treatment with haloperidol (10 nM), haloperidol (10 nM) +
551 quinpirole (50 µM), haloperidol (10 nM) + ω-conotoxin (1 µM) or haloperidol (10 nM) + ω-agatoxin
552 (1 µM). (A) DAT clusters with diameter >75 nm in green, clusters <75 nm in magenta. (B) Dense DAT
553 clusters in red (>80 localizations, radius 50 nm). (C) localizations segmented by Voronoi tessellation.
554 (D, E) Normalized fraction of DAT clusters >75 nm (in %) (D) and normalized fraction of DAT
555 localizations in dense clusters (in %) (E), means ± S.E.; one-way ANOVA, ****p<0.0001, ***p<0.001,
556 **p<0.01, *p<0.05, n.s., not significant. (F) Probability density functions (P.D.F.) (curves color-
557 coded as in the bar diagrams) for the Voronoi tessellated areas averaged by varicosity. Probability
558 density functions (P.D.F.) (curves color-coded as in the bar diagrams) for the Voronoi tessellated

559 areas averaged by varicosity. Data are from 3 cultures and 153 control, 166 haloperidol, 167
560 quinpirole, 178 ω-conotoxin and 176 ω-agatoxin varicosities,
561 (G-R) Single particle tracking dSTORM (SPT-dSTORM) identifies changes in DAT mobility in response to
562 NMDA and D2R antagonism. (G) Example live dSTORM images of DA neurons labeled with the
563 fluorescent cocaine analogue, DG3-80. (H) Boxed region in B. (I) Detected tracks and (J) Distribution
564 of segment lengths in varicosity from control SPT-dSTORM experiment (16 ms frame rate). (K)
565 Example traces of a confined and an unconstrained freely moving particle (DG3-80 labeled DAT).
566 (L) Fraction of unconstrained tracks out of the total number of tracks. Data are means of 23 tracks
567 ± S.E. (M) Probability Density Function (P.D.F.) for total mean jump distances (M.J. D) (i.e. the
568 distance an individual molecule/particle has traveled between each image) for control
569 experiments. (N) P.D.F. when separated into static and freely moving particles. Among the freely
570 moving particles, some moved very fast with M.J.D. of 200-350 nm. (O) NMDA (20 µM, 5 min)
571 increases population of DAT molecules with M.J.D. > 200 nm, which is blunted by AP5 (100 µM). (P)
572 Fraction of fast moving particles (> 200 nm), means ± S.E., data from 13 control, 4 NMDA and 5
573 NMDA+AP5 experiments; (Q, R) The D2R antagonists haloperidol (10 nM, 5 min) and UH-232 (1
574 µM) increase the population of DAT molecules with M.J.D. > 200 nm > 200 nm; M, Fraction of fast
575 moving particles (> 200 nm), means ± S.E., data are from 10 control, 6 haloperidol and 5 UH-232
576 experiments; one-way ANOVA, *p<0.05; **p<0.01, n.s., not significant.
577 See also Figure S5 and Movies S1, S3.
578
579 **Figure 6. DAT nanodomains overlap with PIP2 nanodomains**
580 (A) Example dual-color dSTORM images of phosphatidylinositol 4,5-bisphosphate (PIP2) (red, CF568)
581 and DAT (blue, Alexa647) in a neuronal extension from cultured DA neurons (left) with close-up
582 image of varicosity (right) corresponding to boxed region in the left image.

583 (B) Example dual-color dSTORM images of varicosities from DA neurons showing localizations for PIP2
584 (red) and DAT (blue). Left, Control; Right, neurons exposed to haloperidol (10 nM, 5 min).
585 (C-F) Effect of NMDA and haloperidol on PIP2 clustering. Upper panels, Control, NMDA (20 µM) and
586 NMDA (20 µM) + AP5 (100 µM); Lower panels; Control, haloperidol (10 nM) and haloperidol (10
587 nM) + quinpirole (50 µM). (C) Normalized fraction of PIP2 localizations in large clusters (>75 nm in
588 diameter) (in %) and (D), normalized fraction of PIP2 localizations in dense clusters (>80
589 localizations, radius 50 nm) (in %), means ±S.E., one-way ANOVA, ****p<0.0001, **p<0.01, n.s.,
590 not significant. (E) Probability density functions (P.D.F.) (color-coded as in the bar diagrams) for the
591 Voronoi tessellated areas averaged by varicosity. (F) Probability density functions (P.D.F.) (color-
592 coded as in the bar diagrams) of the association of PIP2 with DAT clusters determined by Voronoi
593 tessellation-based association (see Figure 2) showing strong association PIP2 with DAT. Data are
594 from 3 cultures and 137 control, 126 NMDA, 121 NMDA + AP5 varicosities; and 140 control, 102
595 haloperidol, 67 haloperidol + quinpirole varicosities,
596
597 **Figure 7. The D2R is also distributed into nanodomains**
598 (A) Example dual-color dSTORM images of the D2R (red, CF568) and DAT (blue, Alexa647) in DA
599 neuronal extension (left) with close-up image of varicosity (right) corresponding to boxed region in
600 the left image.
601 (B) Example dual color dSTORM images of varicosities from DA neurons showing localizations for D2R
602 (red) and DAT (blue). Left, Control; Right, neurons exposed to haloperidol (10 nM, 5 min).
603 (C-F) Effect of NMDA and haloperidol on D2R clustering. Upper panels, Control, NMDA (20 µM) and
604 NMDA (20 µM) + AP5 (100 µM); Lower panels; Control, haloperidol (10 nM) and haloperidol (10
605 nM) + quinpirole (50 µM). (C) Normalized fraction of D2R localizations in large clusters (>75 nm in
606 diameter) (in %) and (D), normalized fraction of D2R localizations in dense clusters (>80

607 localizations, radius 50 nm) (in %), means ±S.E., one-way ANOVA, ***p<0.001, **p<0.01, *p<0.05,
608 n.s., not significant. (E) Probability density functions (P.D.F.) (color-coded as in the bar diagrams)
609 for the Voronoi tessellated areas averaged by varicosity. (F) Probability density functions (P.D.F.)
610 (color-coded as in the bar diagrams) of the association of D2R with DAT clusters determined by
611 Voronoi tessellation-based association (see Figure 2). Data are from 3 cultures and data from 3
612 cultures and 112 control, 157 NMDA, 75 NMDA + AP5; and 179 control, 195 haloperidol and 150
613 quinpirole varicosities.
614 See also Figure S5 and S6.
615
616

617 **LEGENDS TO SUPPLEMENTARY FIGURES**

618 **Figure S1. Estimation of protein copy number in DAT clusters (Related to Figure 1.)**

619 (A) To estimate how many DAT molecules that are present in an average DAT nanodomain defined by
620 the DBSCAN analysis, we used a protocol modified from (Ehmann *et al.*, 2014; Siddig *et al.*, 2020)
621 and labeled cultured DA neurons with a twofold dilution row (1:3200-1:100) of primary Mab369
622 DAT antibody, followed by labeling with Alexa647-conjugated secondary antibody and dSTORM
623 imaging. The figures show four example varicosities labeled with lowest level of primary DAT
624 antibody (1/3200 dilution). Individual nanodomains/clusters are shown by separate colors. For
625 each cluster the number of localizations was counted, as shown by the histogram to right of each
626 example.

627 (B) The clustering analysis was performed on 85 varicosities labeled with 1/3200 dilution of primary
628 antibody and the total number of localizations per cluster for the entire set is shown in the left
629 panel. The graph indicates that the minimum number of localizations in a cluster as a conservative
630 estimate is 3 at this extreme antibody dilution and thus that 3 localizations likely may arise from a
631 single primary antibody in this set of images. We next counted the number of localizations found
632 in varicosities labeled with increasing concentrations of primary antibody (1/100, 1/200, 1/400,
633 1/800, 1/1600, 1/3200 as indicated by color) and counted the number of localizations present
634 within clusters that has a diameter greater than 75 nm (right panel). The resulting distributions,
635 shown color-coded, peaked at an estimated 100 localizations. It follows that estimated ~33 copies
636 of the monocolonal antibody would be present that in turn each can label up to two DAT molecules.
637 Accordingly, a rough estimate says that an average cluster contains 50-100 DAT molecules.

638 (C) Example varicosities showing DAT localizations in green in clusters with a diameter larger than 75
639 nm using a 1/100 dilution of primary DAT antibody.

640

641 **Figure S2. Cluster analysis by varied label density cluster verification (Related to Figure 1.)**

642 (A) Example dSTORM images of varicosities from DA neuronal cultures labeled with DAT primary
643 antibody at indicated dilutions.

644 (B) Localization present in clusters (ρ/ρ0) was compared to the relative area of the ROI covered by a
645 cluster mask (η), with each data point being a single varicosity (Baumgart *et al.*, 2016). The red line
646 indicates a reference curve from a random distribution and thus the data strongly support a true
647 clustered distribution of DAT localizations into nanodomains and accordingly that the clustering of
648 the DAT signal observed is not the result of multiple observations of single fluorophores in
649 agreement with our previous data in DAT expressing CAD cells (Rahbek-Clemmensen *et al.*, 2017).

650

651 **Figure S3. Effects of DAT ligands on DAT clustering in transfected CAD cells and DA neurons (Related to**
652 **Figure 2).**

653 (A) Left, Example PALM/TIRF images of the mEOS2 DAT expressed in plasma membrane of CAD cell
654 with and without incubation with an excess of cocaine. The experiment was done while examining
655 DG3-63's association with unclustered DAT where unlabeled cocaine was applied to the CAD cells
656 to compete with DG3-63 signal and to show its specificity. The excess cocaine caused a declustering
657 of DAT. Right, Probability density function (P.D.F.) for the Voronoi tessellated areas averaged by
658 varicosity showing a dramatic reduction in the clustering of DAT following cocaine application. Data
659 from 16 control cells (3 transfections) and 17 treated cells (2 transfections).

660 (B) Example dSTORM images visualizing WT DAT expressed in CAD cells after 10 min treatments with
661 JHW007 (20 µM), nomifensine (20 µM), noribogaine (20 µM) or vehicle (control) prior to fixation.

662 (C) Probability density function (P.D.F.) for the Voronoi tessellated areas showing increased clustering
663 of DAT in response noribogaine, JHW007 and decreased clustering in response to nomifensine.
664 Data from 33 control images, 32 noribogaine images, 35 nomifensine images, and 35 JHW007

665 images. Samples originated from 3 transfections of CAD cells. Curves are means with S.E. indicated
666 by shaded areas.
667 (D) Effect of 5 min treatment of DA primary cultures (prior to fixation and dSTORM imaging) with
668 nomifensine (20 µM), noribogaine (20 µM) or DA (200 nM). Left, Normalized fraction of clusters
669 >75 nm (in %). Right, Normalized fraction of DAT localizations in dense clusters (in %), means ± S.E.;
670 data are from 222 control, 119 nomifensine, 97 noribogaine, and 140 dopamine varicosities
671 obtained in 6 sets of experiments (45 control, 42 nomifensine, 39 noribogaine pictures and 47 DA
672 pictures); one-way ANOVA, ****$p<0.0001$, n.s., not significant.
673
674 **Figure S4. Overexpression in DA neurons of mNaChBac increases while Kir2.1 decreases neuronal**
675 **excitability (Related to Figure 4).**
676 (A-C) Verification of selective expression of bacterial ion channels in DA neurons by a dual viral
677 transduction protocol. The cultured DA neurons were co-infected with an AAV encoding either Cre-
678 dependent mNaChBac or Kir2.1 and with an AAV encoding Cre recombinase under control of a
679 truncated tyrosine hydroxylase (TH) promoter (AAV-pTH-iCre-WPREpA) (see Methods). Images
680 show a putative Kir2.1 expressing DA neuron immunostained for the co-expressed protein mKate2
681 (red) and for DAT (blue). (A) Widefield image with merged DAT and Kir2.1 signal; B, Kir2.1 signal; C,
682 DAT signal.
683 (D) Whole-cell patch-clamp of a DA neuron expressing Kir2.1. Merged image showing IR-DIC and
684 mKate2 signal of a DA neuron and a patch electrode approaching the cell soma.
685 (E) Left, Current-clamp recording mode (at 0 pA) showing increased firing activity of mNaChBac
686 expressing DA neuron (purple) and essentially no firing activity of Kir2.1 expressing DA neuron
687 (black) as compared to control neuron (green). Right, Action potential frequency (Hz) in control

688 (n=6), mNaChBac (n=4), mNaChBacMUT (n=3) and Kir2.1 (n=5) expressing neurons, means ± S.E.;
689 one-way ANOVA with Dunnett's multiple comparison test, **p<0.01.
690
691 **Figure S5. The effect of the D2R antagonist haloperidol on cytosolic Ca^{2+} and synaptotagmin labeling**
692 **in terminals of cultured DA neurons (Related to Figure 5).**
693 (A) Left, Live imaging of terminals from DA neurons expressing the genetically Ca^{2+} sensor jRGECO
694 (three example neurons shown). Right images are enlarged from boxed regions shown in left
695 images. The neurons are, as indicated, shown both immediately before and 200 sec after
696 exposure to 10 nM haloperidol. Right, Averaged fluorescence jRGECO signal over time measured
697 for 6 presynaptic terminals showing how haloperidol (10 nM) cause a rapid rise in cytosolic Ca^{2+}.
698 (B) Haloperidol decreases DAT clustering while increasing synaptotagmin 1 labeling in DAT positive
699 varicosities. DA cultures were incubated prior to fixation and immunolabeling for 10 min in the
700 presence or absence of 10 nM haloperidol with antibody targeting the luminal end of
701 synaptotagmin 1. Left, Representative widefield images of DAT and synaptosome with and without
702 haloperidol treatment. Right, Representative DAT dSTORM images with and without haloperidol
703 treatment. Right images are close-ups of the left images.
704 (C) Left, Normalized fraction of DAT localizations in large clusters (>75 nm in diameter) (in %); Middle,
705 normalized fraction of DAT localizations in dense clusters (>80 localizations, radius 50 nm) (in %);
706 Right, synaptostagmin 1 immunofluorescence per varicosity. Data are means ±S.E. and obtained
707 from 429 control varicosities and 464 haloperidol varicosities, across sets of neuronal cultures, one-
708 way ANOVA, ****p<0.0001, ***p<0.001.
709
710
711

712 **Figure S6. Verification of D2R antibody (Related to Figure 7).**

713 (A) Verification of D2R antibody in transfected heterologous cells. HEK293 cell were transiently
714 transfected with the D2R short isoform or DAT. Widefield microscopy show D2R immunosignal in
715 some but not all HEK 293 cells transiently expressing the D2R short isoform. No signal was observed
716 in DAT expressing HEK cells stained with D2R antibody.

717

718 (B) Verification of D2R antibody in slices from WT and D2R KO mice. Striatal brain slices from D2R KO
719 mice and WT litter mates (Maldonado et al., 1997) were stained for DAT and D2. While a clear
720 immunosignal demarcating striatum was seen for D2 in WT mice, this was absent in the knock-out
721 mice.

722

723 **Figure S7. Analysis of STX-1 and clathrin nanodomains (Related to Figures 6 and 7).**

724 (A) Example dual-color dSTORM images of syntaxin-1 (STX-1) (red, CF56) and DAT (blue, Alexa647)
725 (upper left panels), and clathrin (red, CF56) and DAT (blue, Alexa647) (lower left panels) in DA
726 neuronal extension (left) with close-up of varicosity (right) corresponding to boxed region in left
727 image.

728 (B) Example dual-color dSTORM images of varicosities from DA neurons showing localizations for
729 syntaxin-1 (STX-1) (red, CF56) and DAT (blue, Alexa647) (upper right panels), and clathrin (red,
730 CF56) and DAT (blue, Alexa647) (lower right panels), Left, Control; Right, neurons exposed to NMDA
731 (20 µM, 5 min).

732 (C-J) Effect of NMDA on STX-1 and clathrin clustering. Cultured DA neurons were stimulated with vehicle
733 (control), NMDA (20 µM) or NMDA (20 µM) + AP5 (100 µM) before DAT and STX-1/clathrin
734 immunolabeling for dSTORM analysis. (C, D) Normalized fraction of STX-1 or clathrin localizations
735 in large clusters (>75 nm in diameter) (in %) and (E, F), normalized fraction of STX-1 or clathrin

736 localizations in dense clusters (>80 localizations, radius 50 nm) (in %), means ±S.E., one-way
737 ANOVA, **p<0.01, *p<0.05, n.s., not significant. (G, H) Probability density functions (P.D.F.) (color-
738 coded as in the bar diagrams) for the Voronoi tessellated areas averaged by varicosity (G, STX-1; H,
739 Clathrin). (I, J) Probability density functions (P.D.F.) (color-coded as in the bar diagrams) of the
740 association of of STX-1 or clathrin with DAT clusters determined by Voronoi tessellation-based
741 association (see Figure 2). Data are from 3 cultures and 217 control, 278 NMDA, 183 NMDA + AP5
742 varicosities (STX-1); and 98 control, 98 NMDA, 108 NMDA + AP5 varicosities (clathrin).
743
744 **Figure S8. Validation of the multicolor alignment of our microscope (Related to Star Methods).**
745 To verify the multicolor alignment of our microscope, dSTORM images of 100 nm Tetraspek beads were
746 taken. Localizations were fit to widefield illuminated Tetraspec beads and processed as our dSTORM data
747 is processed. Localization data was generated into images as such to show how well aligned the multicolor
748 signal is in our system.
749
750
751 **LEGENDS TO SUPPLEMENTARY MOVIES**
752 **Movie S1. 3D-STORM of DA neuronal varicosity immunostained for DAT (control conditions) (Related**
753 **to Figures 4 and 5).** Color-code is based on density where red localizations are defined as over 300
754 localizations within 100 nm radius, white as ~150 localizations within a 100 nm radius, and the
755 remainder in blue.
756
757 **Movie S2. 3D-STORM representation of DA neuronal varicosity immunostained for DAT (5 min NMDA**
758 **treatment) (Related to Figures 4 and 5).** Color-code is based on density where red localizations are

759 defined as over 300 localizations within 100 nm radius, white as ~150 localizations within a 100
760 nm radius, and the remainder in blue.
761
762 **Movie S3. 3D-STORM representation of DA neuronal varicosity immunostained for DAT (5 min**
763 **haloperidol treatment) (Related to Figure 5).** Color-code is based on density where red localizations
764 are defined as over 300 localizations within 100 nm radius, white as ~150 localizations within a
765 100 nm radius, and the remainder in blue.

766 **STAR*METHODS**

767 **LEAD CONTACT**

768 Further information and requests for resources and reagents should be directed to and will be fulfilled by

769 the Lead Contact, Ulrik Gether (gether@sund.ku.dk)

770

771 **MATERIALS AVAILABILITY**

772 All unique reagents generated in this study are available from the Lead Contact. Plasmids generated are

773 available upon request.

774

775 **DATA AND CODE AVAILABILITY**

776 Custom written codes used for the data analysis can be found at: https://github.com/GetherLab/Super-

777 Resolution-Data-Analysis. The datasets supporting the current study have not been deposited in a public

778 repository because of the file size but are available from the corresponding author on request.

779

780 **EXPERIMENTAL MODEL AND SUBJECT DETAILS**

781 **Primary cultures of DA neurons with cortical glia cells**

782 Cultured glial cells were obtained from cortex and cultured DA neurons were obtained from the midbrain

783 of P1-P3 Wistar rats (Charles River, Germany). Gender was mixed as the cultures were generated from a

784 mixed sex populations of rat pups. For preparation of cultured glial cells, brains were removed from

785 euthanized P1-P3 pups and placed in phosphate-buffered saline (PBS) on ice. The cortex of each brain was

786 isolated and cut into millimeter sized sections and collected in cold dissection medium (Hanks' Balanced

787 Salt Solution with added Sodium Pyruvate (1 mM), Penicillin-Streptomycin (Sigma P0781, 200 U/L), 10

788 mM HEPES, and 0.54% glucose)). After collecting all, the dissection medium was replaced with glia cell

789 medium (DMEM with HEPES "1965", FBS (10%), Penicillin-Streptomycin (60 U/L)). The tissue was

790 mechanically titrated through pipetting up and down using a flame-polished Pasteur pipette followed by
791 straining through a 70 µm cell trainer and centrifugation for 10 min at 200-300 x g. The pellet was
792 resuspended in 10 mL glia medium and strained again before a second centrifugation for 10 min at 200-
793 300 g and removal of the supernatant. The pellet was resuspended and seeded into large T175 flasks at
794 approximately 1.5 brains per flask with added glial medium to a total of 20 mL. Glia cells were grown in
795 an incubator at 37◦ C with 5% CO_2 until they were 70% confluent. The cells were either frozen in heat-
796 inactivated serum containing 10% DMSO for later use or applied to ethanol-cleaned and poly-D-lysine-
797 coated coverslips and incubated for 1 week prior to DA neuron addition. On the day before DA neuron
798 addition, the glial cells were changed to DA neuron medium (Neurobasal A with heat-inactivated FBS
799 (1/100), GlutaMAX (1/100) B-27 (1/50), ascorbic acid (200 µM), Penicillin-Streptomycin (60 U/L),
800 kynurenic acid (0.5 mM)). Midbrain DA neurons were generated using a protocol modified from (Rayport
801 *et al.*, 1992). Brains from rat pups (P1-P3) were isolated and placed in PBS on ice. Midbrain sections were
802 retrieved from each brain as the brains were cut while in dissection buffer. The midbrain sections were
803 transferred to papain solution (cysteine (1 mM), DNase (0.1 mg/mL), papain (20 units/mL), NaCl (116
804 mM), KCl (5.4 mM), $CaCl_2$ (1.9 mM), NaHCO3 (26 mM), $NaH_2PO_4H_2O$ (2 mM), $MgSO_4$ (1 mM), EDTA (0.5
805 mM), Glucose (25 mM), kynurenic acid (0.5 mM) in water) for 30 min at 37◦C. The solution was replaced
806 with prewarmed DA medium and samples were mechanically titrated with flame polished Pasteur
807 pipettes and the resulting suspension centrifuged at 200-300 x g for 10 min. The pellet was resuspended
808 in DA neuron medium and applied to each culture. Glia-derived neurotrophic factor (GDNF) (100ng/mL
809 of culture solution volume) was applied immediately after seeding of the neurons. Cultures were
810 incubated for 2 to 3 weeks prior to use. All procedures were performed according to institutional
811 guidelines at the Faculty of Health Sciences, University of Copenhagen.
812
813

814 **Mouse brain slices**

815 Mouse brain slices were obtained from male C57BL/6 mice 12-16 weeks old. The slices were prepared as
816 described in Methods Details. For validation of D2 receptor antibody, slices were obtained from D2
817 receptor knock-out mice and WT littermates (Maldonado *et al.*, 1997). All procedures were performed
818 according to institutional guidelines at the Faculty of Health and Medical Sciences, University of
819 Copenhagen.

820

821 **Heterologous cell culture**

822 Cath.a-differentiated (CAD) cells (Qi et al., 1997) (ATCC CRL-11179 or Sigma-Aldrich 08100805),
823 originating from mouse (B6/D2 F1 hybrid) catecholaminergic neuronal tumor. The cells were maintained
824 in a 1:1 mixture of DMEM 1965 and Ham's F-12 medium (Invitrogen), both supplemented with 10% FBS
825 and 0.01 mg/mL gentamicin. HEK293 cells (human embryonic kidney cells, ATCC CRL-1573) were grown
826 as described (Hansen *et al.*, 2014).

827

828 **METHOD DETAILS**

829 **Molecular biology, virus generation and virus transduction**

830 The cDNA encoding human DAT (synthetic gene kindly provided by Dr. Jonathan Javitch, Columbia
831 University, NY, USA (Loland et al., 2004) was inserted into pmEOS2-C1 (RRID: Addgene#54510) to
832 generate pmEOS2-hDAT C1 encoding hDAT with mEOS2 fused to the N-terminus. Plasmids encoding WT
833 hDAT and D421N hDAT (pRC/CMV hDAT and pRC/CMV hDAT D421N) were generated as described
834 (Herborg *et al.*, 2018)). The cDNA encoding the short transcriptional variant of human DA D2 receptor
835 with an N-terminal FLAG tag (SF-D2R-S) was inserted into mammalian expression vector pcDNA 3.1(+)
836 (Invitrogen) (Klewe et al., 2008). The Cre-dependent construct, pAAV-CAG-Flex-NES-jRGECO1a-WPREpA,
837 was obtained from Addgene (RRID: Addgene #100854). The plasmids, pAAV-hSyn-DIO-mNaChBac-T2A-

838 mKate2-WPREpA, pAAV-hSyn-DIO-mNaChBacMUT-T2A-mKate2-WPREpA and pAAV-hSyn-DIO-Kir2.1-
839 T2A-mKate2-WPREpA (Lin *et al.*, 2010; Xue *et al.*, 2014), were SLIC cloned (Jeong et al., 2012) from pAAV-
840 EF1α-F-FLEX-mNaChBac-T2A-tdTomato (RRID: Addgene #60658) and pAAV-EF1α-F-FLEX-Kir2.1-T2A-
841 tdTomato (RRID: Addgene #60661), respectively, into a Cre-dependent AAV backbone plasmid with a
842 mKate2 fluorophore instead of tdTomato. This was done to make them sufficiently short so that packaging
843 into an AAV capsid would be feasible (ITR to ITR length<4700 kbp). The pAAV-pTH-iCre-
844 WPREpA construct was created and cloned in-house and contains a truncated 488bp rat TH promoter
845 encoding Cre recombinase. In-house generated AAVs were produced using a FuGene6 (Promega)
846 mediated triple plasmid co-transfection method in HEK293t cells. Three days after transfection, cells were
847 harvested and virus purified using an adapted Iodixanol gradient purification protocol (Matsui et al.,
848 2012). Genomic AAV titer was determined by a PicoGreen-based method as described elsewhere (Piedra
849 et al., 2015). AAV2-retro-pTH-iCre mediated expression of Cre-dependent jRGECO1 was verified by
850 fluorescence microscopy and no differences were observed across the different titers used. For
851 transduction, the appropriate virus was applied to primary culture DA neurons at an approximate
852 concentration of 2*10E9 vg/mL at 1 to 3 days after preparation of the neuronal cultures.
853
854 **Transfection of DA neurons**
855 Primary cultures of DA neurons were transfected using Magnetotransfection at ~14 DIV (Underhill et al.,
856 2014). NeuroMag reagent (OZ biosciences) (8 µL) was mixed with plasmid (4 µg) and DA neuron medium
857 (200 µL). The mixture was incubated for 20 min at RT before it was added to cultures grown in 6-well
858 plates. The culture was positioned on top of a magnetic plate for 15 min after which the culture before it
859 was moved back to the cell incubator and used for immunostaining 24-48 hours later.
860
861

862 **Immunostaining of primary cultures of DA neurons for dSTORM and PALM**

863 The cell samples were fixed in paraformaldehyde (3%) and washed three times in glycine (20 mM) and
864 NH_4Cl (50 mM) in PBS. Subsequently, the cells were washed in blocking buffer (5% Donkey serum, 1% BSA
865 in PBS), and incubated in blocking permeabilization buffer (blocking buffer with saponin (0.2%)). Primary
866 antibody was applied in blocking buffer for 60 min, followed by 3–5 min incubation in blocking buffer.
867 Secondary antibody was applied in blocking buffer for 45 min, and the sample was incubated 2x for 5 min
868 in blocking buffer. Samples were washed in PBS twice and post-fixated in paraformaldehyde (3%) for 15
869 min. Samples were washed twice in glycine (20 mM) and NH_4Cl (50 mM) in PBS and stored in PBS at 4°C
870 until imaging.

871 The synaptotagmin 1 feeding experiment was performed as defined by (Truckenbrodt *et al.*, 2018).
872 Live DA primary cultures were exposed to synaptotagmin 1 antibody (SS 105 311, Synaptic Systems) at a
873 1:120 dilution from a 1 mg/mL solution together with haloperidol (10 nM) or vehicle 37°C for one hour.
874 The cultures were carefully washed with 37°C aCSF while avoiding exposure to air before fixation and
875 immunolabeling per the primary culture staining protocol.

876

877 **Preparation and immunostaining of mouse brain slices for dSTORM**

878 Mice were anesthetized with isoflurane and perfused first with PBS followed by 4% paraformaldehyde
879 (PFA) injected directly into the heart. Brains were then placed in 4% PFA for 24 hours, followed by sucrose
880 (30%) for 24 to 48 hours. Subsequently, brains were snap-frozen on powdered dry ice and stored at -
881 80°C. The brains were sliced using a cryostat (Leica CM3050 S) to obtain 10 µm striatal coronal sections
882 and each slice was immediately fused to a 3-aminopropyltriethoxysilane coated coverslip and let dry at
883 room temperature before being stored in antifreeze (50% glycerol 50% PBS) at -20 ◦C. For
884 immunostaining, brain sections were first rinsed 3x in PBS and subsequently washed 2x with 15 min
885 incubation in glycine (20 mM) and NH_4Cl (50 mM) in PBS. This was followed by 30 min wash in 10 mM

886 trisodium citrate, pH 6.0, preheated to 80◦ C, 4x wash in PBS and then blocking/permeabilization for 30
887 min in PBS with 5% donkey serum, 1% BSA and 0.3 % Triton X-100. Primary antibody was applied overnight
888 in blocking/permeabilization buffer followed by washing in 5/5/90 min increments and application of
889 secondary antibody overnight in blocking/permeabilization buffer. Sections were again washed in 5/5/90
890 minute increments in blocking/permeabilization buffer and then with 5/5 min increments with PBS. The
891 sections were post-fixated in paraformaldehyde (3%) and washed twice for 15 min in glycine (20 mM) and
892 NH_4Cl (50 mM) in PBS. Samples were lastly washed twice in PBS and stored in PBS at 4 ◦C until imaging.
893
894 **Antibodies and labeling**
895 Secondary antibodies (donkey anti-rat, Jackson 712-005-153, RRID:AB_2340631; donkey anti-mouse,
896 Jackson 715-005-151, RRID:AB_2340759); or donkey anti-rabbit, Jackson 711-005-152,
897 RRID:AB_2340585) were labeled with either NHS-ester conjugated Alexa647 or CF™568 (Biotium,
898 Freemont, CA) and then isolated through Zeba™ Spin Desalting Columns, 40K MWCO (ThermoFisher
899 87767). This was completed by first washing the column 3x with 300 µL of 100 mM $NaHCO_3$ in PBS.
900 Following the washes, 50 µg of antibody in 100 µL of PBS was added and spun at 1500 x g for 2 mins. The
901 flow-through was collected and combined with a 5-fold molar excess of NHS ester fluorophore. This
902 solution was incubated in the dark at RT, shaking, for 2.5 hours. A new spin column was then washed 3
903 times with NaN--3 (0.02%) in PBS. The antibody sample with the dye was then added to the column and
904 centrifuged for 2 min at 1500 x g. The protein concentration and label concentration of the final product
905 were measured on a NanoDrop 2000 Spectrophotometer (ThermoFisher). Labeled antibodies had
906 between 1 and 2 fluorophores attached.
907
908
909

910 We used the following antibodies and fluorophores for our imaging analysis:

Antibody Target	Product Number	Experiment	Dilution	Secondary antibody	Fluorophore
DAT	Millipore MAB369 RRID:AB_2190413	Primary culture dSTORM	1/200	5 µg/mL Donkey anti-Rat	Alexa647
DAT	Millipore MAB369 RRID:AB_2190413	IHC dSTORM	1/200	10 µg/mL Donkey anti-Rat	Alexa647
DAT	Millipore MAB369 RRID:AB_2190413	Expansion (ExM)	1/200	5 µg/mL Donkey anti-Rat	Atto 643
TH	Millipore MAB318 RRID:AB_2201528	PALM/dSTORM	1/500	5 µg/mL Donkey anti-Mouse	Alexa647
STX-1	Synaptic Systems 110 011 RRID:AB_887844	Primary culture dSTORM	1/500	5 µg/mL Donkey anti-Mouse	CF568
Clathrin light chain	Synaptic Systems 113 011 RRID:AB_887706	Primary culture dSTORM	1/500	5 µg/mL Donkey anti-Mouse	CF568
PIP2	Abcam ab11039 RRID:AB_442848	Primary culture dSTORM	1/500	5 µg/mL Donkey anti-mouse	CF568
D2R	Synaptic Systems 376 205 RRID:AB_2636918	Primary culture dSTORM	1/500	5 µg/mL Donkey anti-rabbit	CF568
mKate2	Evrogen AB233 RRID:AB_2571743	Primary culture dSTORM	1/500	5 µg/mL Donkey anti-rabbit	CF568
Synapto-tagmin 1 (luminal domain)	Synaptic systems 105 311 RRID:AB_10805653	Active varicosity detection	1/125	5 µg/mL Donkey anti-Mouse	Alexa 488

911
912

913 **Expansion Microscopy (ExM)**

914 For ExM, perfused brains were acquired by injecting first PBS and then 4% PFA into the heart of
915 anesthetized mice. Brains were postfixated in 4% PFA for 24 hours and immersed in sucrose solution
916 (30%) for 24 to 48 hours. Coronal brain slices (40 µm) were obtained with a cryostat. The brain slices were
917 stored, free floating, in antifreeze (50% glycerol 50% PBS) at -20◦C until use. Brain slices were washed
918 with PBS three times, and then permeabilized in blocking buffer (5% donkey serum, 1% bovine serum
919 albumin, 0.1% Triton X-100, in PBS). Brain slices were incubated overnight with primary antibody in
920 blocking buffer (5% donkey serum, 1% bovine serum albumin, 0.1% Triton X-100, in PBS, pH 7.4). Slices

921 were washed 4x in blocking buffer with 30 min increments and incubated overnight with secondary
922 antibody in blocking buffer at 4◦C. Slices were again washed 4x in blocking buffer with 30 min increments.
923 Anchoring treatment was performed with Acryloyl-X-SE (0.1 mg/mL) in PBS at room temperature
924 overnight (Truckenbrodt *et al.*, 2019). Gel solution was made by mixing N,N-dimethylacrylamide (1.335 g)
925 and sodium acrylate (0.32g) in 2.85 g of water. Oxygen was purged with nitrogen gas for 40 min. 2.7 mL
926 of the gelling solution were mixed with 0.3 mL 0.036 g/mL solution of potassium persulfate ($K_2S_2O_8$)
927 solution and purged of oxygen with nitrogen gas for 15 min on ice. Brain slices were transferred to the
928 extra gelling solution and placed flat on poly-D-Lysine coated glass slides. . Excess gelling solution was
929 removed, and glass coverslips were placed on the edges of each slice to limit gel dispersion. All work from
930 this point was done in a cold room (4◦C). Aliquots of 500 µL of polymerization solution were combined
931 with 2 µL of TEMED was added and the solution vortexed before applying 80 µL to brain slices. A layer of
932 parafilm covered coverslip was placed overtop of the gel to fully surround the gel. The sample was kept
933 in the cold room for 15 min before being brought back out to room temperature. The container with the
934 gels was filled with nitrogen and wet paper to keep humidity and made airtight. Following gelation,
935 samples were carefully cut out from the chamber in a sim-card shape to ensure orientation. Gels were
936 measured in size, and placed in digestion buffer overnight at room temperature (50mM TRIS, 800 mM
937 guanidine HCl, 2 mM CaCl2, 0.5% Triton X-100, proteinase K 8U/mL, pH 8.0). The gels were placed into
938 individual dishes and dialyzed with water many times over a day until they no longer expanded. Imaging
939 was performed the next day on a spinning disk confocal microscope (FEI CorrSight utilizing a C-
940 Apochromat 63x/1.20 W Corr M27 objective). Samples were places dry on poly-D-Lysine coated chambers
941 and water was added to the top of the gel just enough so the gel was hydrated but not so it would move
942 around.
943
944

945 **dSTORM**

946 For dSTORM we used a buffer containing β-mercaptoehtanol and an enzymatic oxygen scavenger system
947 (10% (w/V) glucose, 1% (V/V) beta-mercaptoethanol, 2 mM cyclooctatetraene, 50 mM Tris-HCl (pH 8), 10
948 mM NaCl, 34 µg mL^{-1} catalase, 28 µg mL^{-1} glucose oxidase). The imaging was performed with an ECLIPSE
949 Ti-E epifluoresence/TIRF microscope (NIKON, Japan) equipped with 405 nm, 488 nm 561, and 647 nm
950 lasers (Coherent, California, USA). All lasers are individually shuttered and collected in a single fiber to the
951 sample through a 1.49 NA, 100x, apochromat TIRF oil objective (NIKON). Single color imaging was done
952 with a dichroic mirror (z405/488/561/647 rpc) and the emitted light was filtered by a 710/80 nm bandpass
953 filter. For dual-color dSTORM, we used a dichroic mirror with the range 350–412, 485–490, 558–564, and
954 637–660 nm (97,335 QUAD C-NSTORM C156921). The excitation light was filtered at the wavelengths:
955 401 ± 24 nm, 488 ± 15 nm, 561 ±15 nm, 647 ± 24 nm. The emitted light was filtered at the wavelengths:
956 425-475, 505-545, 578-625, and 664-787 nm, and secondly by an extra filter to decrease noise (561 nm
957 Longpass, Edge Basic, F76-561, AHF). A motorized piezo stage controlled by a near-infrared light-adjusted
958 perfect focus system (NIKON) is applied to the system to reduce any sample drift over time in the z-
959 direction. Single-color dSTORM images were constructed from 30,000 frames taken at a 16 ms frame rate.
960 Dual-color dSTORM images were constructed from 20,000 frames for each color taken at a 16 ms frame
961 rate with each color alternating by frame. Photons were collected with an iXon3 897 EM-CCD camera
962 camera (Andor, United Kingdom). Laser powers used were 2.3 kW cm −2 for 647 nm, 1.0 kW cm−2 for
963 488 nm and for 561 nm. The 405 nm laser was used to incrementally increase blinking behavior at power
964 <0.1 kW cm−2. For 3D-dSTORM, a cylindrical lens was placed before the camera to impart astigmatism.

965

966

967

968

969 **PALM**

970 For PALM imaging of mEos-DAT, we obtained 5,000 consecutive frames with a frame rate of 33 Hz to
971 construct one image. The 488 nm excitation laser was held constant, 0.4 kW cm^{-2}, during the capture of
972 the image while the 405 nm activation laser was gradually increased to <0.1 kW cm^{-2}.

973

974 **Localization fitting of dSTORM data**

975 2D localizations were fit with ThunderSTORM using local maximum detection with a threshold of 1.5
976 *std(Wave.F1) and estimator of an integrated gaussian PSF. Sigma was 1.6, fit radius was 3 pixels, and
977 weighted least squares was the method to fit the estimated gaussian to the PSF (Ovesny et al., 2014). 3D
978 localization fitting was performed with fit3Dcspline (Li *et al.*, 2018). 3D calibrations were made on 100 nm
979 TetraSpeck beads attached to a coverslip by first placing 50 µL of MgCl2 (1M) on the coverslip and then
980 adding 500 L of water with 0.9 µL of TetraSpeck beads to the coverslip. Drift for all data was corrected
981 with redundant cross correlation through Matlab (Wang et al., 2014). Localizations were filtered for
982 uncertainty being less than 25 nm and then merged for localizations that were detected within 15 nm and
983 3 frames.

984

985 **Data processing pipeline - dSTORM**

986 To perform necessary localization fitting on the 1349 dSTORM images included in this study, an in-house
987 data processing pipeline was developed to streamline operations. Localizations were fit to the raw data
988 with the aforementioned settings in ThunderSTORM through a self-written ImageJ macro. Although
989 ThunderSTORM can perform the remaining processing steps, a custom python script (utilizing Matlab
990 functions) was written to perform cross correlation, merging and filtering so that redundant cross
991 correlation could be employed. The images were then blinded by labeling them with a random integer
992 and saving the cypher elsewhere. Through a separate custom Matlab script, varicosities were selected

993 from each image though a freehand selection. Varicosities were identified by the local swelling of their
994 structure compared to the rest of the extension. We next used DBSCAN (density based spatial clustering
995 of applications with noise) (Ester *et al.*, 1996; Rahbek-Clemmensen *et al.*, 2017) to identify clusters by size
996 or for determining localizations in dense clusters through the use of a python script employing the
997 DBSCAN method from the sklearn python library. Voronoi tessellation (Levet *et al.*, 2019) was employed
998 through Matlab. The Voronoi based density association algorithm was also written in house and using
999 Matlab.
1000
1001 **Varicosity identification in dSTORM DA neuron culture data**
1002 Automatic varicosity identification could not discern between extension and varicosity, so these were
1003 selected through a freehand ROI taken of blinded files. Localization data for all images in a given dataset
1004 were blinded by being randomly assigned a number that was stored on a cypher. ROIs were then gathered
1005 without the knowledge of the image identity, with this information restored in the analysis of the ROIs.
1006
1007 **Varicosity identification in brain slice dSTORM data**
1008 As this was a computationally intensive process, each image was divided into 100 quadrants in a 10x10
1009 grid. Within each quadrant, the localizations were sub-sampled down to 1000 random localizations, and
1010 the Voronoi tessalation was obtained for that section. Tesselated areas were filtered for having an area
1011 less than 15000 nm^2. Tesselated shapes that were touching one another were merged together. Shapes
1012 were now filtered for possessing an area greater than 300000 nm^2. These ROIS were buffered by 50 nm
1013 along each edge to smooth the ROI.
1014
1015
1016

1017 **Clustering analysis of dSTORM data**

1018 Cluster size was identified by performing DBSCAN on each varicosity for a radius of 15 nm and 5
1019 localizations being the cluster qualifier. The convex hull was gathered for each cluster to find its area, and
1020 the fraction of clusters with a diameter >75 nm was used for the cluster size analysis. Cluster size
1021 distributions were not shown as clusters reaching the detection limit of this method are not accurate and
1022 cause a false perception on the cluster size distribution. Localizations in dense clusters were found by
1023 applying DBSCAN to each varicosity with a radius of 50 nm and 80 localizations being the qualifier. Voronoi
1024 tessellation was applied to each varicosity and areas were filtered for sizes between 5 nm2 and 1000 nm2.
1025 Probability density functions were created for these distributions.

1026

1027 **Density Association**

1028 Density association was found by performing Voronoi tessellation on target A, and finding all points in
1029 target B that were 25 nm from any point in target A. Each of these target B points that possessed A
1030 association were mapped to the Voronoi tessellated area from target A they resided in. The probability
1031 density functions for target A and the areas from target A that had an associated target B were created.
1032 This procedure was applied to compare the dSTORM signal of DG3_63 to mEOS2-DAT, STX1 to DAT, D2R
1033 to DAT, PIP2 to DAT, and clathrin to DAT.

1034

1035 **Quantification of DAT molecules in nanodomains**

1036 Primary DA neurons were labeled and imaged for dSTORM with the DAT MAB369 antibody at dilutions
1037 1:200, 1:400, 1:800, 1:1600, 1:3200. Varicosities were manually selected from blinded data files. Clusters
1038 of localizations potentially arising from single localizations were identified in the varicosities found in the
1039 1:3200 dilution data set through DBSCAN with the parameters [ε = 30 nm, nps = 2]. A histogram was made
1040 comparing the number of localizations found per cluster from this cluster analysis, and 3 localizations was

1041 determined to be the estimate for the number of localizations arising from a single monoclonal antibody
1042 in this image set. Clusters were then found in the remaining dataset through the same method defined
1043 to identify cluster size. A histogram was made to show the number of localizations present within the
1044 clusters found with a diameter >75 nm. The peak of this histogram was ~100 localizations, suggesting
1045 there are roughly 33 primary antibodies labeling DAT within a given cluster/nanodomain of this size.
1046

1047 **Varied label density cluster verification**

1048 Varicosities used for the counting experiment were subject to the varied label density cluster verification
1049 test (Baumgart *et al.*, 2016). Sig for gaussians was set to 15 nm and the cut gauss at x times sig was set to
1050 2. The threshold selected was 2.
1051

1052 **Labeling and imaging primary cultures with DG3-63**

1053 Live primary cultures were labeled with DG3-63 (20 nM) (Guthrie *et al.*, 2020) for 10 min in the dark at
1054 room temperature and washed 3 times with aCSF (NaCl (120 mM), KCl (5 mM), $CaCl_2$ (2 mM), $MgCl_2$ (2
1055 mM), 1 mM NaH_2PO_4, HEPES (25 mM), glucose (30 mM), pH 7.4). Samples were fixed with
1056 paraformaldehyde (3%) for 15 min followed by 3 washes with glycine (20 mM) and NH_4Cl (50 mM) in PBS.
1057 Samples were imaged in normal dSTORM buffer.
1058

1059 **Transfection of CAD cells, labeling with DG3-63 and pharmacological treatments**

1060 CAD cells were transfected with pmEOS2-hDAT encoding mEOS-DAT or with pRC/CMV-hDAT or pRC/CMV-
1061 hDAT D421N encoding WT DAT and the DAT mutant D421N, respectively (Herborg *et al.*, 2018). The CAD
1062 cells (~1 million cells) were seeded the day before transfection in a 25 cm^2 flask and washed on the day
1063 of transfection before addition of 5 mL of medium. For the transfection, 1 µg of DNA was added to 100
1064 µL of optiMEM as well as 3 µL Lipofectamine (Invitrogen) to a separate 100 µL of optiMEM. After 5 min,

1065 the two solutions were mixed and incubated for 30 min before the total mixture was added to the cells.
1066 The next day the cells were harvested and seeded on poly-D-Lysine coated coverslips (100,000 cells per
1067 coverslip). For DG3-63 labeling experiments, the media was removed the next day from the mEOS-DAT
1068 expressing cells and 1 mL of aCSF was added (NaCl (120 mM), KCl (5 mM), $CaCl_2$ (2 mM), $MgCl_2$ (2 mM),
1069 HEPES (25 mM), glucose (30 mM), pH 7.4) before incubation for 10 min with or without 100 µM unlabeled
1070 cocaine. Following this, the cells were labeled with 10 nM DG3-63 (Guthrie *et al.*, 2020) for 10 min in aCSF.
1071 Samples were washed 3 times with aCSF and then fixed for 15 min in paraformaldehyde (3%) followed by
1072 2x wash with glycine (20 mM) and NH_4Cl (50 mM) in PBS. Samples were imaged in dSTORM buffer as
1073 described above. For dSTORM of hDAT WT and D421N, cells the cover slips samples were stained in the
1074 same fashion as primary DA cultures. For pharmacology experiments, CAD cells expressing WT DAT were
1075 treated with nomifensine (20 µM), noribogaine (20 µM), JHW007 (20 µM) or vehicle for 10 minutes prior
1076 to fixation.
1077
1078 **Pharmacological treatment of acute brain slices**
1079 Mice were euthanized with isoflurane and the live brains were removed. Coronal sections, 300 µm thick,
1080 were cut with a vibratome in cold aCSF (NaCl (119 mM), KCl (2.5 mM), NaH_2PO_4 (24 mM), Glucose (12.5
1081 mM), $CaCl_2$ (2 mM), $MgCl_2$ (2 mM)) that was being aerated with carbogen gas. Brain slices were
1082 transferred to aCSF and maintained for 1 hour at room temperature under constant carbogenation. Slices
1083 were then transferred to either aCSF or aCSF with AP5 (100 µM), both at 37◦ C for 10 min. Slices from
1084 normal aCSF were moved to aCSF with or without NMDA (20 µM). The NMDA containing aCSF had
1085 reduced magnesium (0.3 mM MgCl2) and added glycine (100 µM). The samples from AP5 were
1086 transferred to aCSF with AP5 (100 µM) and NMDA (20µM), reduced magnesium (0.3 mM $MgCl_2$), and
1087 added glycine (100 µM). These incubated for 5 min, and then the slices were transferred to
1088 paraformaldehyde (3%) overnight at 4◦ C. Slices were transferred to a 30% sucrose solution for 2 days a

1089 4◦C and then placed into plastic molds and covered with Tissue-Tek O.C.T. and stored at -80◦C. Samples
1090 were sliced at 10 µm on the cryostat and stained for dSTORM.
1091
1092 **Pharmacological treatment of primary cultures**
1093 In general, treatments were performed by replacing the media at room temperature with aCSF (NaCl (120
1094 mM), KCl (5 mM), $CaCl_2$ (2 mM), $MgCl_2$ (2 mM), 1 mM NaH_2PO_4, HEPES (25 mM), glucose (30 mM), pH 7.4)
1095 followed by stimulation with indicated compounds. For the NMDA or haloperidol experiments with
1096 testing of VGCC inhibitors, cells were treated for 10 min with either control aCSF, AP5 (100 µM) or
1097 quinpirole (50 µM), ω-conotoxin (1 µM), ω-agatoxin (1 µM). Samples were then treated for 5 min with
1098 these same concentrations as cotreatment with either NMDA (20 µM) or haloperidol (10 nM). NMDA
1099 treatments were done in aCSF with added glycine (100 µM). All experiments using NMDA were done with
1100 aCSF with reduced magnesium (0.3 mM $MgCl_2$) for all conditions. For the BAPTA-AM experiment, the
1101 pretreatment with BAPTA-AM (25 µM) was for 30 min prior to the 5-min NMDA (20 µM) treatment. For
1102 the DAT pharmacology experiments, the neurons were treated for 5 minutes with either nomifensine (10
1103 µM), noribogane (20 µM) or dopamine (200 nM) prior to fixation.
1104
1105 **SPT-dSTORM**
1106 Live primary cultures were labeled with DG3-80 (20 nM) for 10 min and then washed 3 times with aCSF
1107 (NaCl (120 mM), KCl (5 mM), $CaCl_2$ (2 mM), $MgCl_2$ (2 mM – 0.3 mM for NMDA related experiments), 1 mM
1108 NaH_2PO_4, HEPES (25 mM), glucose (30 mM), pH 7.4). A suitable location to image was found while the
1109 sample was kept in aCSF, and then SPTdSTORM imaging was done in a modified dSTORM buffer (560
1110 µg/mL glucose oxidase, 34 µg/mL catalase, 1.4 µL/mL β-Mercaptoethanol in aCSF). Pharmacological
1111 treatment were done 5 min before imaging with either 20 µM NMDA with 100 µM glycine, 200 nM
1112 haloperidol, or 1 µM UH-232. AP5 (100 µM) was applied for 10 min prior to cotreatment with NMDA.

1113 Imaging was performed at room temperature on the NIKON TiE Eclipse TIRF microscope described under
1114 dSTORM. Light with a wavelength of 561 nm at 0.3 kW cm^{-2} was utilized to promote blinking of the
1115 fluorophores. Images were collected with 16 ms frame rate. Localizations were fit using ThunderStorm as
1116 described above. Single molecule trajectories were found using the program swift (Turkowyd et al., 2020).
1117 Parameter used beyond the default were: ”expdisplacement” : 300,”expnoiserate”:
1118 10,”maxblinkingduration” : 2,”pblink” : 0.5,”preappear” : 0.5,”pswitch” : 0.001,”precision”:
1119 30,”pruningbase” : 2,”pruningrate” : 0.2,”randomseed” : 42,”wdiffusion” : 2,”wdirected” : 1,”wfield” :
1120 0,”wimmobile” : 1.
1121
1122 **Electrophysiology recordings of DA neurons**
1123 DA neuronal cultures were transduced after 3 DIV (days in vitro) with pAAV-pTH-iCre-WPREpA plus either
1124 pAAV-hSyn-DIO-mNaChBac-T2A-mKate2-WPREpA, pAAV-hSyn-DIO-mNaChBacMUT-T2A-mKate2-
1125 WPREpA or pAAV-hSyn-DIO-Kir2.1-T2A-mKate2-WPREpA. Electrophysiological recording by the whole-
1126 cell patch clamp technique were done 2-3 weeks after transduction. The DA neurons expressing either
1127 mNaChBac or Kir2.1 were identified based on mKate2 fluorescence using an upright microscope (Olympus
1128 BX51WI). For the recordings, the cultures were submerged in circulating, heated, and oxygenated aCSF
1129 (in mM; NaCl 125, KCl 2.5, $NaHCO_3$ 26, $CaCl_2$ 2, $MgCl_2$ 1, NaH_2PO_4 1.25, Glucose 25; 2 ml/min, 35°C). The
1130 aCSF was supplemented with NBQX (20 µM). The patch glass electrode was filled with (in mM) K-
1131 gluconate 122, Na_2-ATP 5, $MgCl_2$ 2.5, $CaCl_2$ 0.0003, Mg-Gluconate 5.6, K-Hepes 5, H-Hepes 5, and EGTA 1,
1132 and had tip resistance of 4-6 MΩ. After break-in, the cells were held at 0 pA in current clamp mode to
1133 measure the pacemaker activity. Recordings were acquired with a Multiclamp 700B amplifier and 1440A
1134 Digitizer.
1135
1136

1137 **Calcium Imaging of DA neurons**

1138 Primary DA neurons were prepared as described above but instead of culturing the neurons on glass
1139 coverslips, they were cultured on MatTek 35 mm 14 mm glass microwell (no 1.5) glass bottom dishes
1140 (MatTek). To enable measurement of Ca^{2+}-fluctuations specifically in DA neurons, the neurons were
1141 transduced with an AAV encoding double-floxed jRGECO1a (AAV-CAG-Flex-NES-jRGECO1a-WPREpA)
1142 together with an AAV encoding Cre recombinase under control of a truncated TH promoter (AAV2-retro-
1143 pTH-iCre-WPREpA). The cell medium was changed to aCSF (NaCl (120 mM), KCl (5 mM), CaCl2 (2 mM),
1144 $MgCl_2$ (2 mM), 1 mM NaH_2PO_4, HEPES (25 mM), glucose (30 mM), pH 7.4) immediately prior to imaging.
1145 Imaging took place at room temperature on the NIKON TiE Eclipse TIRF microscope described above. Once
1146 a suitable neuron was located, the sample was imaged with 561 nm light (10 W cm^{-2}). Videos were
1147 collected with a 16 ms frame rate. Haloperidol was added mid-video so that the sample had a total
1148 concentration of 10 nM Haloperidol. Data was collected from three independent experiments. Two
1149 varicosities were identified per image.

1150

1151 **RNA-seq mining and data analysis**

1152 All RNA sequencing data was accessed via the Gene Expression Omnibus (GEO) under the following
1153 accession numbers: GSE108020, GSE115070, GSE76381, GSE116470, GSE116138. Raw counts were
1154 converted to RPKM and quantile normalized using the preprocessCore (3.11) package in R.

1155

1156 **Quantification and Statistical Analysis**

1157 Statistical details can be found in the figure legends and were computed with GraphPad Prism 8. When
1158 employing one-way ANOVA, Dunnett's post hoc test was used for multiple comparisons. The dSTORM
1159 comparisons were normalized to the control sample from the individual imaging session. This was done
1160 to control for unavoidable variability in sample preparations and between imaging sessions.

Experiment	Number of sample preparations	Number of dSTORM Images	Number of varicosities (neuron experiments) or cells (CAD cell experiment)
IHC dSTORM NMDA	3	102	4028
CAD Cell D421N	3	55	80
Membrane Potential	5	186	849
NMDA and VGCC	3	188	841
Haloperidol and VGCC	3	180	840
BAPTA-AM	3	95	208
STX1 NMDA	4	162	678
Clathrin NMDA	3	90	304
PIP2 Haloperidol	3	84	309
PIP2 NMDA	3	88	384
D2 NMDA	3	101	344
D2 Haloperidol	3	90	524
CAD cell pharmcology	3	179	213
Neuron pharmacology	3	237	926
Synaptotagmin uptake	5	122	893

1161

1162

1163

1164 **REFERENCES**

1165 Baker, S.M., Buckheit, R.W., 3rd, and Falk, M.M. (2010). Green-to-red photoconvertible fluorescent
1166 proteins: tracking cell and protein dynamics on standard wide-field mercury arc-based microscopes.
1167 BMC Cell Biol *11*, 15.

1168 Baumgart, F., Arnold, A.M., Leskovar, K., Staszek, K., Folser, M., Weghuber, J., Stockinger, H., and Schutz,
1169 G.J. (2016). Varying label density allows artifact-free analysis of membrane-protein nanoclusters. Nat
1170 Methods *13*, 661-664.

1171 Beckstead, M.J., Grandy, D.K., Wickman, K., and Williams, J.T. (2004). Vesicular dopamine release elicits
1172 an inhibitory postsynaptic current in midbrain dopamine neurons. Neuron *42*, 939-946.

1173 Belovich, A.N., Aguilar, J.I., Mabry, S.J., Cheng, M.H., Zanella, D., Hamilton, P.J., Stanislowski, D.J.,
1174 Shekar, A., Foster, J.D., Bahar, I., et al. (2019). A network of phosphatidylinositol (4,5)-bisphosphate
1175 (PIP2) binding sites on the dopamine transporter regulates amphetamine behavior in Drosophila
1176 Melanogaster. Molecular Psychiatry.

1177 Bermingham, D.P., and Blakely, R.D. (2016). Kinase-dependent Regulation of Monoamine
1178 Neurotransmitter Transporters. Pharmacol Rev *68*, 888-953.

1179 Betzig, E., Patterson, G.H., Sougrat, R., Lindwasser, O.W., Olenych, S., Bonifacino, J.S., Davidson, M.W.,
1180 Lippincott-Schwartz, J., and Hess, H.F. (2006). Imaging intracellular fluorescent proteins at nanometer
1181 resolution. Science *313*, 1642-1645.

1182 Beuming, T., Kniazeff, J., Bergmann, M.L., Shi, L., Gracia, L., Raniszewska, K., Newman, A.H., Javitch, J.A.,
1183 Weinstein, H., Gether, U., and Loland, C.J. (2008). The binding sites for cocaine and dopamine in the
1184 dopamine transporter overlap. Nat Neurosci *11*, 780-789.

1185 Binda, F., Dipace, C., Bowton, E., Robertson, S.D., Lute, B.J., Fog, J.U., Zhang, M., Sen, N., Colbran, R.J.,
1186 Gnegy, M.E., et al. (2008). Syntaxin 1A interaction with the dopamine transporter promotes
1187 amphetamine-induced dopamine efflux. Mol Pharmacol *74*, 1101-1108.

1188 Bjorklund, A., and Dunnett, S.B. (2007). Dopamine neuron systems in the brain: an update. Trends
1189 Neurosci *30*, 194-202.

1190 Bolan, E.A., Kivell, B., Jaligam, V., Oz, M., Jayanthi, L.D., Han, Y., Sen, N., Urizar, E., Gomes, I., Devi, L.A.,
1191 et al. (2007). D2 receptors regulate dopamine transporter function via an extracellular signal-regulated
1192 kinases 1 and 2-dependent and phosphoinositide 3 kinase-independent mechanism. Mol Pharmacol *71*,
1193 1222-1232.

1194 Borroto-Escuela, D.O., Perez De La Mora, M., Manger, P., Narvaez, M., Beggiato, S., Crespo-Ramirez, M.,
1195 Navarro, G., Wydra, K., Diaz-Cabiale, Z., Rivera, A., et al. (2018). Brain Dopamine Transmission in Health
1196 and Parkinson's Disease: Modulation of Synaptic Transmission and Plasticity Through Volume
1197 Transmission and Dopamine Heteroreceptors. Front Synaptic Neurosci *10*, 20.

1198 Buchmayer, F., Schicker, K., Steinkellner, T., Geier, P., Stübiger, G., Hamilton, P.J., Jurik, A., Stockner, T.,
1199 Yang, J.-W., Montgomery, T., et al. (2013). Amphetamine actions at the serotonin transporter rely on
1200 the availability of phosphatidylinositol-4,5-bisphosphate. Proceedings of the National Academy of
1201 Sciences of the United States of America *110*, 11642-11647.

1202 Carquin, M., D'Auria, L., Pollet, H., Bongarzone, E.R., and Tyteca, D. (2016). Recent progress on lipid
1203 lateral heterogeneity in plasma membranes: From rafts to submicrometric domains. Progress in Lipid
1204 Research *62*, 1-24.

1205 Castro-Hernandez, J., Afonso-Oramas, D., Cruz-Muros, I., Salas-Hernandez, J., Barroso-Chinea, P.,
1206 Moratalla, R., Millan, M.J., and Gonzalez-Hernandez, T. (2015). Prolonged treatment with pramipexole
1207 promotes physical interaction of striatal dopamine D3 autoreceptors with dopamine transporters to
1208 reduce dopamine uptake. Neurobiol Dis *74*, 325-335.

1209 Chen, F., Tillberg, P.W., and Boyden, E.S. (2015). Optical imaging. Expansion microscopy. Science *347*,
1210 543-548.

1211 Choquet, D., and Hosy, E. (2020). AMPA receptor nanoscale dynamic organization and synaptic
1212 plasticities. Curr Opin Neurobiol *63*, 137-145.

1213 Das, A.K., Kudlacek, O., Baumgart, F., Jaentsch, K., Stockner, T., Sitte, H.H., and Schutz, G.J. (2019).
1214 Dopamine transporter forms stable dimers in the live cell plasma membrane in a phosphatidylinositol
1215 4,5-bisphosphate-independent manner. J Biol Chem *294*, 5632-5642.

1216 Descarries, L., Watkins, K.C., Garcia, S., Bosler, O., and Doucet, G. (1996). Dual character, asynaptic and
1217 synaptic, of the dopamine innervation in adult rat neostriatum: a quantitative autoradiographic and
1218 immunocytochemical analysis. J Comp Neurol *375*, 167-186.

1219 Ehmann, N., van de Linde, S., Alon, A., Ljaschenko, D., Keung, X.Z., Holm, T., Rings, A., DiAntonio, A.,
1220 Hallermann, S., Ashery, U., et al. (2014). Quantitative super-resolution imaging of Bruchpilot
1221 distinguishes active zone states. Nat Commun *5*, 4650.

1222 Eriksen, J., Jorgensen, T.N., and Gether, U. (2010). Regulation of dopamine transporter function by
1223 protein-protein interactions: new discoveries and methodological challenges. J Neurochem.

1224 Ester, M., Kriegel, H.-P., Sander, J., and Xu, X. (1996). A density-based algorithm for discovering clusters
1225 in large spatial databases with noise. In Proc. 2nd International Conference on Knowledge Discovery and
1226 Data Mining, (AAAI Press), pp. 226–231.

1227 German, C.L., Baladi, M.G., McFadden, L.M., Hanson, G.R., and Fleckenstein, A.E. (2015). Regulation of
1228 the Dopamine and Vesicular Monoamine Transporters: Pharmacological Targets and Implications for
1229 Disease. Pharmacol Rev *67*, 1005-1024.

1230 Giguere, N., Delignat-Lavaud, B., Herborg, F., Voisin, A., Li, Y., Jacquemet, V., Anand-Srivastava, M.,
1231 Gether, U., Giros, B., and Trudeau, L.E. (2019). Increased vulnerability of nigral dopamine neurons after
1232 expansion of their axonal arborization size through D2 dopamine receptor conditional knockout. PLoS
1233 Genet *15*, e1008352.

1234 Goncalves, J., Bartol, T.M., Camus, C., Levet, F., Menegolla, A.P., Sejnowski, T.J., Sibarita, J.B., Vivaudou,
1235 M., Choquet, D., and Hosy, E. (2020). Nanoscale co-organization and coactivation of AMPAR, NMDAR,
1236 and mGluR at excitatory synapses. Proc Natl Acad Sci U S A *117*, 14503-14511.

1237 Groc, L., and Choquet, D. (2020). Linking glutamate receptor movements and synapse function. Science
1238 *368*.

1239 Guthrie, D.A., Klein Herenbrink, C., Lycas, M.D., Ku, T., Bonifazi, A., DeVree, B.T., Mathiasen, S., Javitch,
1240 J.A., Grimm, J.B., Lavis, L., et al. (2020). Novel Fluorescent Ligands Enable Single-Molecule Localization
1241 Microscopy of the Dopamine Transporter. ACS Chem Neurosci *11*, 3288-3300.

1242 Hamilton, P.J., Belovich, A.N., Khelashvili, G., Saunders, C., Erreger, K., Javitch, J.A., Sitte, H.H.,
1243 Weinstein, H., Matthies, H.J., and Galli, A. (2014). PIP2 regulates psychostimulant behaviors through its
1244 interaction with a membrane protein. Nat Chem Biol *10*, 582-589.

1245 Hansen, F.H., Skjorringe, T., Yasmeen, S., Arends, N.V., Sahai, M.A., Erreger, K., Andreassen, T.F., Holy,
1246 M., Hamilton, P.J., Neergheen, V., et al. (2014). Missense dopamine transporter mutations associate
1247 with adult parkinsonism and ADHD. J Clin Invest *124*, 3107-3120.

1248 Heilemann, M., van de Linde, S., Schuttpelz, M., Kasper, R., Seefeldt, B., Mukherjee, A., Tinnefeld, P.,
1249 and Sauer, M. (2008). Subdiffraction-resolution fluorescence imaging with conventional fluorescent
1250 probes. Angew Chem Int Ed Engl *47*, 6172-6176.

1251 Herborg, F., Andreassen, T.F., Berlin, F., Loland, C.J., and Gether, U. (2018). Neuropsychiatric disease-
1252 associated genetic variants of the dopamine transporter display heterogeneous molecular phenotypes. J
1253 Biol Chem *293*, 7250-7262.

1254 Hong, W.C., and Amara, S.G. (2010). Membrane cholesterol modulates the outward facing conformation
1255 of the dopamine transporter and alters cocaine binding. J Biol Chem *285*, 32616-32626.

1256 Huang, B., Bates, M., and Zhuang, X. (2009). Super-resolution fluorescence microscopy. Annu Rev
1257 Biochem *78*, 993-1016.

1258 Hwang, J., Tamm, L.K., Bohm, C., Ramalingam, T.S., Betzig, E., and Edidin, M. (1995). Nanoscale
1259 complexity of phospholipid monolayers investigated by near-field scanning optical microscopy. Science
1260 *270*, 610-614.

1261 Iversen, L.L. (1975). Dopamine receptors in the brain. Science *188*, 1084-1089.

1262 Jeong, J.Y., Yim, H.S., Ryu, J.Y., Lee, H.S., Lee, J.H., Seen, D.S., and Kang, S.G. (2012). One-step sequence-
1263 and ligation-independent cloning as a rapid and versatile cloning method for functional genomics
1264 studies. Appl Environ Microbiol *78*, 5440-5443.

1265 Kasture, A., El-Kasaby, A., Szollosi, D., Asjad, H.M.M., Grimm, A., Stockner, T., Hummel, T., Freissmuth,
1266 M., and Sucic, S. (2016). Functional Rescue of a Misfolded Drosophila melanogaster Dopamine
1267 Transporter Mutant Associated with a Sleepless Phenotype by Pharmacological Chaperones. J Biol Chem
1268 *291*, 20876-20890.

1269 Klewe, I.V., Nielsen, S.M., Tarpo, L., Urizar, E., Dipace, C., Javitch, J.A., Gether, U., Egebjerg, J., and
1270 Christensen, K.V. (2008). Recruitment of beta-arrestin2 to the dopamine D2 receptor: insights into anti-
1271 psychotic and anti-parkinsonian drug receptor signaling. Neuropharmacology *54*, 1215-1222.

1272 Kristensen, A.S., Andersen, J., Jorgensen, T.N., Sorensen, L., Eriksen, J., Loland, C.J., Stromgaard, K., and
1273 Gether, U. (2011). SLC6 neurotransmitter transporters: structure, function, and regulation. Pharmacol
1274 Rev *63*, 585-640.

1275 Kuzhikandathil, E.V., Yu, W.F., and Oxford, G.S. (1998). Human dopamine D3 and D2L receptors couple
1276 to inward rectifier potassium channels in mammalian cell lines. Molecular and Cellular Neuroscience *12*,
1277 390-402.

1278 Lebowitz, J.J., Pino, J.A., Mackie, P.M., Lin, M., Hurst, C., Divita, K., Collins, A.T., Koutzoumis, D.N.,
1279 Torres, G.E., and Khoshbouei, H. (2019). Clustered Kv2.1 decreases dopamine transporter activity and
1280 internalization. J Biol Chem *294*, 6957-6971.

1281 Lee, F.J., Pei, L., Moszczynska, A., Vukusic, B., Fletcher, P.J., and Liu, F. (2007). Dopamine transporter cell
1282 surface localization facilitated by a direct interaction with the dopamine D2 receptor. Embo J *26*, 2127-
1283 2136.

1284 Levet, F., Julien, G., Galland, R., Butler, C., Beghin, A., Chazeau, A., Hoess, P., Ries, J., Giannone, G., and
1285 Sibarita, J.B. (2019). A tessellation-based colocalization analysis approach for single-molecule
1286 localization microscopy. Nat Commun *10*, 2379.

1287 Li, Y.M., Mund, M., Hoess, P., Deschamps, J., Matti, U., Nijmeijer, B., Sabinina, V.J., Ellenberg, J., Schoen,
1288 I., and Ries, J. (2018). Real-time 3D single-molecule localization using experimental point spread
1289 functions. Nat. Methods *15*, 367-+.

1290 Lin, C.-W., Sim, S., Ainsworth, A., Okada, M., Kelsch, W., and Lois, C. (2010). Genetically increased cell-
1291 intrinsic excitability enhances neuronal integration into adult brain circuits. Neuron *65*, 32-39.

1292 Liu, C., and Kaeser, P.S. (2019). Mechanisms and regulation of dopamine release. Curr Opin Neurobiol
1293 *57*, 46-53.

1294 Loland, C.J., Desai, R.I., Zou, M.F., Cao, J., Grundt, P., Gerstbrein, K., Sitte, H.H., Newman, A.H., Katz, J.L.,
1295 and Gether, U. (2008). Relationship between conformational changes in the dopamine transporter and
1296 cocaine-like subjective effects of uptake inhibitors. Mol Pharmacol *73*, 813-823.

1297 Loland, C.J., Granas, C., Javitch, J.A., and Gether, U. (2004). Identification of intracellular residues in the
1298 dopamine transporter critical for regulation of transporter conformation and cocaine binding. J Biol
1299 Chem *279*, 3228-3238.

1300 Maidorn, M., Olichon, A., Rizzoli, S.O., and Opazo, F. (2019). Nanobodies reveal an extra-synaptic
1301 population of SNAP-25 and Syntaxin 1A in hippocampal neurons. Mabs *11*, 305-321.

1302 Maldonado, R., Saiardi, A., Valverde, O., Samad, T.A., Roques, B.P., and Borrelli, E. (1997). Absence of
1303 opiate rewarding effects in mice lacking dopamine D2 receptors. Nature *388*, 586-589.

1304 Manley, S., Gillette, J.M., Patterson, G.H., Shroff, H., Hess, H.F., Betzig, E., and Lippincott-Schwartz, J.
1305 (2008). High-density mapping of single-molecule trajectories with photoactivated localization
1306 microscopy. Nat Methods *5*, 155-157.

1307 Maxfield, F.R., and McGraw, T.E. (2004). Endocytic recycling. Nature Reviews Molecular Cell Biology *5*,
1308 121-132.

1309 McLaughlin, S., and Murray, D. (2005). Plasma membrane phosphoinositide organization by protein
1310 electrostatics. Nature *438*.

1311 Meiergerd, S.M., Patterson, T.A., and Schenk, J.O. (1993). D2 receptors may modulate the function of
1312 the striatal transporter for dopamine - kinetic evidence from studies in-vitro and in-vivo. Journal of
1313 Neurochemistry *61*, 764-767.

1314 Newman, A.H., Cao, J., Keighron, J.D., Jordan, C.J., Bi, G.H., Liang, Y., Abramyan, A.M., Avelar, A.J.,
1315 Tschumi, C.W., Beckstead, M.J., et al. (2019). Translating the atypical dopamine uptake inhibitor
1316 hypothesis toward therapeutics for treatment of psychostimulant use disorders.
1317 Neuropsychopharmacology *44*, 1435-1444.

1318 Ovesny, M., Krizek, P., Borkovec, J., Svindrych, Z., and Hagen, G.M. (2014). ThunderSTORM: a
1319 comprehensive ImageJ plug-in for PALM and STORM data analysis and super-resolution imaging.
1320 Bioinformatics *30*, 2389-2390.

1321 Padmanabhan, P., Bademosi, A.T., Kasula, R., Lauwers, E., Verstreken, P., and Meunier, F.A. (2020).
1322 Need for speed: Super-resolving the dynamic nanoclustering of syntaxin-1 at exocytic fusion sites.
1323 Neuropharmacology *169*.

1324 Parsons, L.H., Schad, C.A., and Justice, J.B. (1993). Coadministration of the d2 antagonist pimozide
1325 inhibits up-regulation of dopamine release and uptake induced by repeated cocaine. Journal of
1326 Neurochemistry *60*, 376-379.

1327 Pereira, D.B., Schmitz, Y., Meszaros, J., Merchant, P., Hu, G., Li, S., Henke, A., Lizardi-Ortiz, J.E.,
1328 Karpowicz, R.J., Jr., Morgenstern, T.J., et al. (2016). Fluorescent false neurotransmitter reveals
1329 functionally silent dopamine vesicle clusters in the striatum. Nat Neurosci *19*, 578-586.

1330 Prasad, B.M., and Amara, S.G. (2001). The dopamine transporter in mesencephalic cultures is refractory
1331 to physiological changes in membrane voltage. J Neurosci *21*, 7561-7567.

1332 Qi, Y., Wang, J.K., McMillian, M., and Chikaraishi, D.M. (1997). Characterization of a CNS cell line, CAD, in
1333 which morphological differentiation is initiated by serum deprivation. J Neurosci *17*, 1217-1225.

1334 Rahbek-Clemmensen, T., Lycas, M.D., Erlendsson, S., Eriksen, J., Apuschkin, M., Vilhardt, F., Jorgensen,
1335 T.N., Hansen, F.H., and Gether, U. (2017). Super-resolution microscopy reveals functional organization
1336 of dopamine transporters into cholesterol and neuronal activity-dependent nanodomains. Nat Commun
1337 *8*, 740.

1338 Ramamoorthy, S., Shippenberg, T.S., and Jayanthi, L.D. (2011). Regulation of monoamine transporters:
1339 Role of transporter phosphorylation. Pharmacol Ther *129*, 220-238.

1340 Rayport, S., Sulzer, D., Shi, W.X., Sawasdikosol, S., Monaco, J., Batson, D., and Rajendran, G. (1992).
1341 Identified postnatal mesolimbic dopamine neurons in culture: morphology and electrophysiology. J
1342 Neurosci *12*, 4264-4280.

1343 Robertson, S.D., Matthies, H.J., and Galli, A. (2009). A closer look at amphetamine-induced reverse
1344 transport and trafficking of the dopamine and norepinephrine transporters. Mol Neurobiol *39*, 73-80.

1345 Salamone, A., Zappettini, S., Grilli, M., Olivero, G., Agostinho, P., Tome, A.R., Chen, J., Pittaluga, A.,
1346 Cunha, R.A., and Marchi, M. (2014). Prolonged nicotine exposure down-regulates presynaptic NMDA
1347 receptors in dopaminergic terminals of the rat nucleus accumbens. Neuropharmacology *79*, 488-497.

1348 Shivanandan, A., Deschout, H., Scarselli, M., and Radenovic, A. (2014). Challenges in quantitative single
1349 molecule localization microscopy. FEBS Lett *588*, 3595-3602.

1350 Siddig, S., Aufmkolk, S., Doose, S., Jobin, M.-L., Werner, C., Sauer, M., and Calebiro, D. (2020). Super-
1351 resolution imaging reveals the nanoscale organization of metabotropic glutamate receptors at
1352 presynaptic active zones. Science Advances *6*, eaay7193.

1353 Sorkina, T., Richards, T.L., Rao, A., Zahniser, N.R., and Sorkin, A. (2009). Negative regulation of dopamine
1354 transporter endocytosis by membrane-proximal N-terminal residues. J Neurosci *29*, 1361-1374.

1355 Spyraki, C., and Fibiger, H.C. (1981). Intravenous self-administration of nomifensine in rats: implications
1356 for abuse potential in humans. Science *212*, 1167-1168.

1357 Strange, P.G. (2008). Antipsychotic drug action: antagonism, inverse agonism or partial agonism. Trends
1358 Pharmacol Sci *29*, 314-321.

1359 Suh, B.C., and Hille, B. (2008). PIP2 is a necessary cofactor for ion channel function: how and why? Annu
1360 Rev Biophys *37*, 175-195.

1361 Thal, L.B., Tomlinson, I.D., Quinlan, M.A., Kovtun, O., Blakely, R.D., and Rosenthal, S.J. (2019). Single
1362 Quantum Dot Imaging Reveals PKCbeta-Dependent Alterations in Membrane Diffusion and Clustering of
1363 an Attention-Deficit Hyperactivity Disorder/Autism/Bipolar Disorder-Associated Dopamine Transporter
1364 Variant. ACS Chem Neurosci *10*, 460-471.

1365 Tillberg, P.W., Chen, F., Piatkevich, K.D., Zhao, Y., Yu, C.C., English, B.P., Gao, L., Martorell, A., Suk, H.J.,
1366 Yoshida, F., et al. (2016). Protein-retention expansion microscopy of cells and tissues labeled using
1367 standard fluorescent proteins and antibodies. Nat Biotechnol *34*, 987-992.

1368 Torres, G.E. (2006). The dopamine transporter proteome. J Neurochem *97 Suppl 1*, 3-10.

1369 Torres, G.E., and Amara, S.G. (2007). Glutamate and monoamine transporters: new visions of form and
1370 function. Curr Opin Neurobiol *17*, 304-312.

1371 Tritsch, N.X., and Sabatini, B.L. (2012). Dopaminergic modulation of synaptic transmission in cortex and
1372 striatum. Neuron *76*, 33-50.

1373 Truckenbrodt, S., Sommer, C., Rizzoli, S.O., and Danzl, J.G. (2019). A practical guide to optimization in
1374 X10 expansion microscopy. Nat Protoc *14*, 832-863.

1375 Truckenbrodt, S., Viplav, A., Jahne, S., Vogts, A., Denker, A., Wildhagen, H., Fornasiero, E.F., and Rizzoli,
1376 S.O. (2018). Newly produced synaptic vesicle proteins are preferentially used in synaptic transmission.
1377 EMBO J *37*.

1378 Turkowyd, B., Schreiber, S., Wortz, J., Segal, E.S., Mevarech, M., Duggin, I.G., Marchfelder, A., and
1379 Endesfelder, U. (2020). Establishing Live-Cell Single-Molecule Localization Microscopy Imaging and
1380 Single-Particle Tracking in the Archaeon Haloferax volcanii. Front Microbiol *11*, 583010.

1381 Turner, T.J., Adams, M.E., and Dunlap, K. (1993). Multiple Ca2+ channel types coexist to regulate
1382 synaptosomal neurotransmitter release. Proceedings of the National Academy of Sciences of the United
1383 States of America *90*, 9518-9522.

1384 Underhill, S.M., Wheeler, D.S., Li, M., Watts, S.D., Ingram, S.L., and Amara, S.G. (2014). Amphetamine
1385 modulates excitatory neurotransmission through endocytosis of the glutamate transporter EAAT3 in
1386 dopamine neurons. Neuron *83*, 404-416.

1387 van den Bogaart, G., Meyenberg, K., Risselada, H.J., Amin, H., Willig, K.I., Hubrich, B.E., Dier, M., Hell,
1388 S.W., Grubmuller, H., Diederichsen, U., and Jahn, R. (2011). Membrane protein sequestering by ionic
1389 protein-lipid interactions. Nature *479*, 552-555.

1390 Wang, Y., Schnitzbauer, J., Hu, Z., Li, X., Cheng, Y., Huang, Z.L., and Huang, B. (2014). Localization events-
1391 based sample drift correction for localization microscopy with redundant cross-correlation algorithm.
1392 Opt Express *22*, 15982-15991.

1393 Xue, M., Atallah, B.V., and Scanziani, M. (2014). Equalizing excitation-inhibition ratios across visual
1394 cortical neurons. Nature *511*, 596-600.

1395 Zapata, A., Kivell, B., Han, Y., Javitch, J.A., Bolan, E.A., Kuraguntla, D., Jaligam, V., Oz, M., Jayanthi, L.D.,
1396 Samuvel, D.J., et al. (2007). Regulation of dopamine transporter function and cell surface expression by
1397 D3 dopamine receptors. J Biol Chem *282*, 35842-35854.

1398

Figure 1

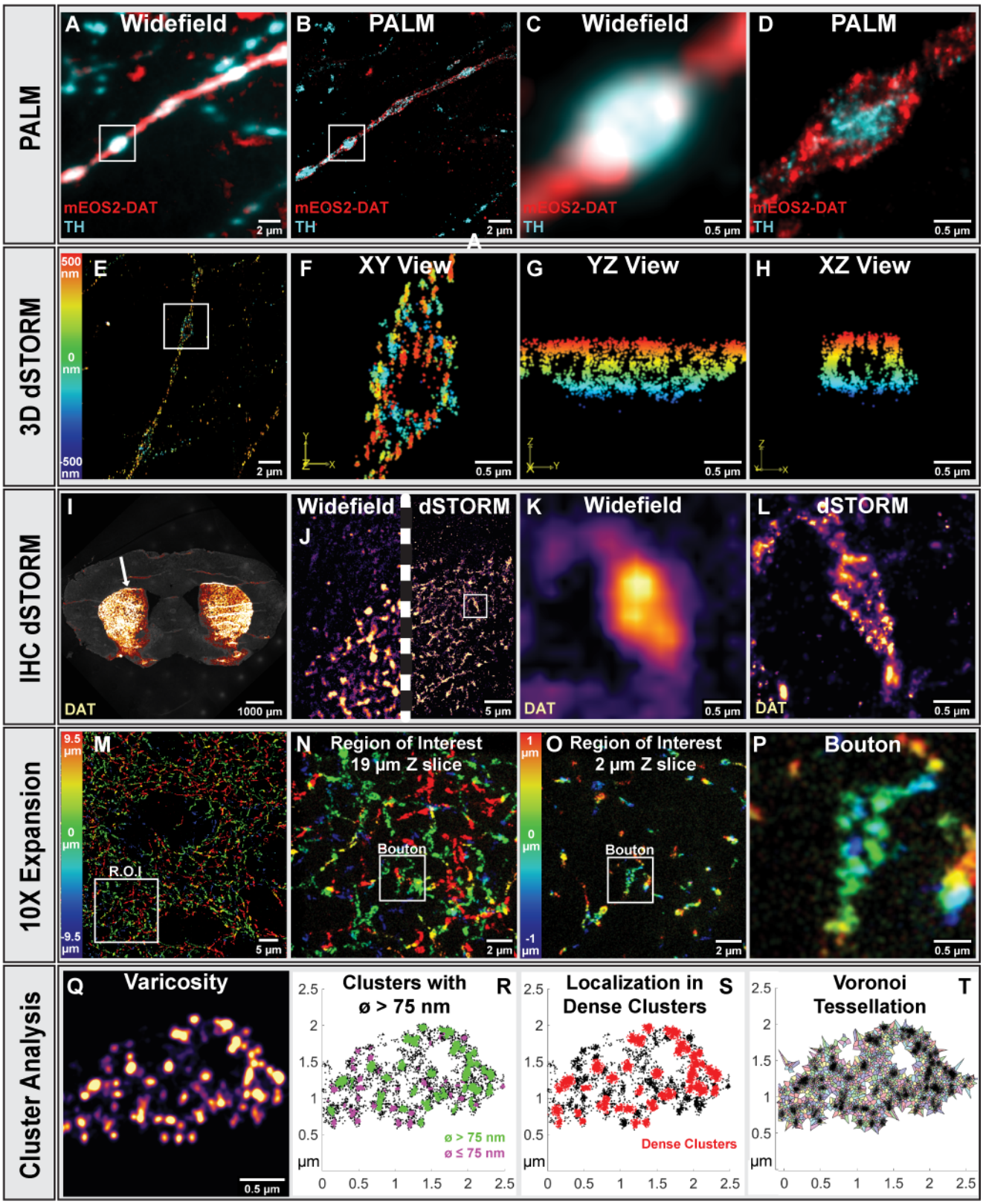
PALM
A Widefield
B PALM
C Widefield
D PALM
mEOS2-DAT
TH
2 µm
0.5 µm
3D dSTORM
500 nm
0 nm
-500 nm
E
F XY View
G YZ View
H XZ View
IHC dSTORM
I
DAT
1000 µm
Widefield
dSTORM
J
5 µm
K Widefield
L dSTORM
10X Expansion
9.5 µm
0 µm
-9.5 µm
M
R.O.I
N Region of Interest 19 µm Z slice
Bouton
O Region of Interest 2 µm Z slice
1 µm
-1 µm
P Bouton
Cluster Analysis
Q Varicosity
Clusters with ø > 75 nm
R
ø > 75 nm
ø ≤ 75 nm
Localization in Dense Clusters
S
Dense Clusters
Voronoi Tessellation
T
µm
0
0.5
1
1.5
2
2.5

Figure 2

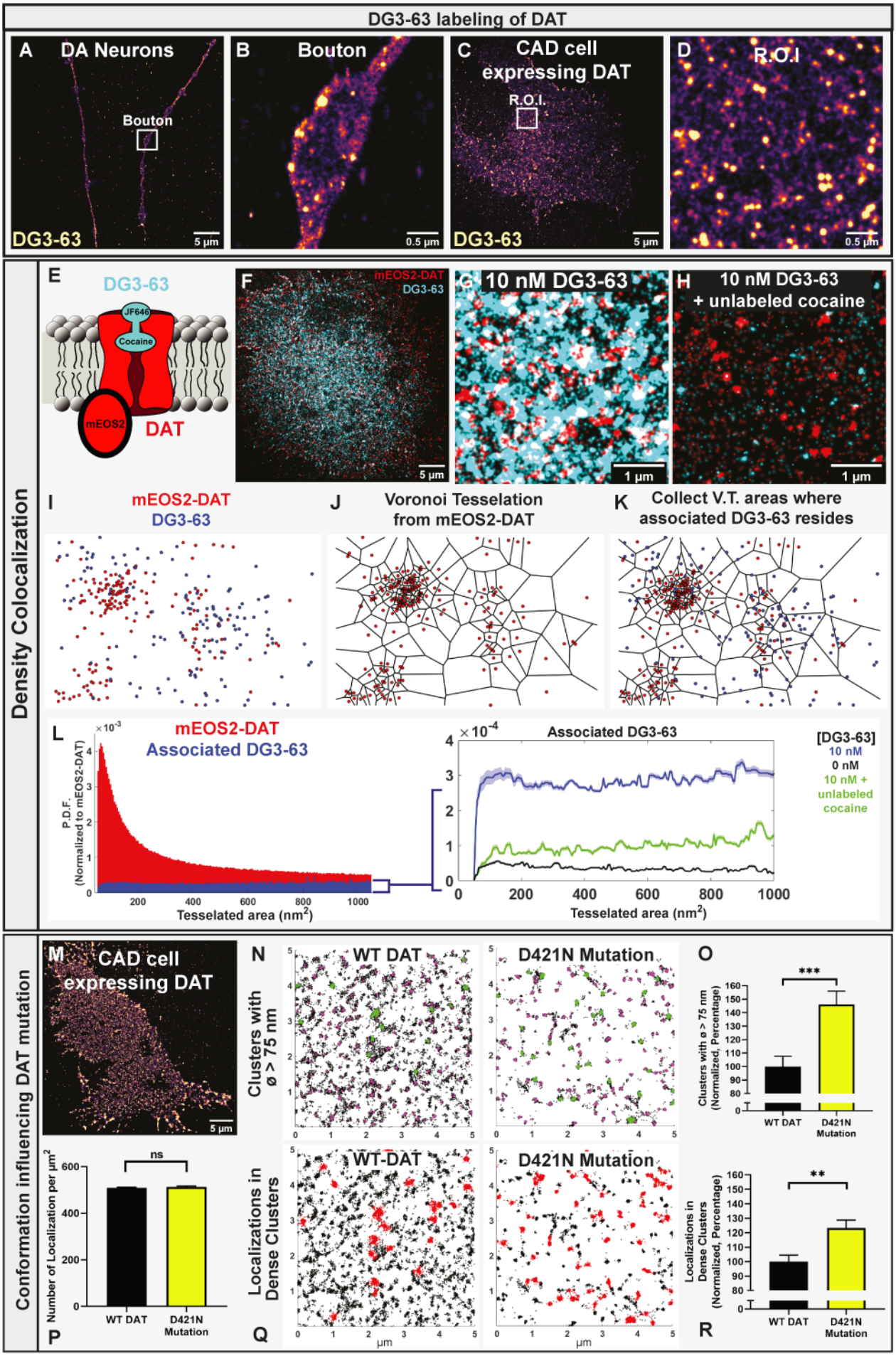
DG3-63 labeling of DAT
A DA Neurons
Bouton
DG3-63
5 µm
B Bouton
0.5 µm
C CAD cell expressing DAT
R.O.I.
DG3-63
5 µm
D R.O.I
0.5 µm
Density Colocalization
E
DG3-63
JF646
Cocaine
mEOS2
DAT
F
mEOS2-DAT
DG3-63
5 µm
G 10 nM DG3-63
1 µm
H 10 nM DG3-63 + unlabeled cocaine
1 µm
I mEOS2-DAT DG3-63
J Voronoi Tesselation from mEOS2-DAT
K Collect V.T. areas where associated DG3-63 resides
L
mEOS2-DAT
Associated DG3-63
P.D.F. (Normalized to mEOS2-DAT)
Tesselated area (nm²)
Associated DG3-63
[DG3-63]
10 nM
0 nM
10 nM + unlabeled cocaine
Conformation influencing DAT mutation
M CAD cell expressing DAT
5 µm
N
WT DAT
D421N Mutation
Clusters with ø > 75 nm
O
Clusters with ø > 75 nm (Normalized, Percentage)
WT DAT
D421N Mutation
P
Number of Localization per µm²
ns
WT DAT
D421N Mutation
Q
WT-DAT
D421N Mutation
Localizations in Dense Clusters
µm
R
Localizations in Dense Clusters (Normalized, Percentage)
WT DAT
D421N Mutation

Figure 3

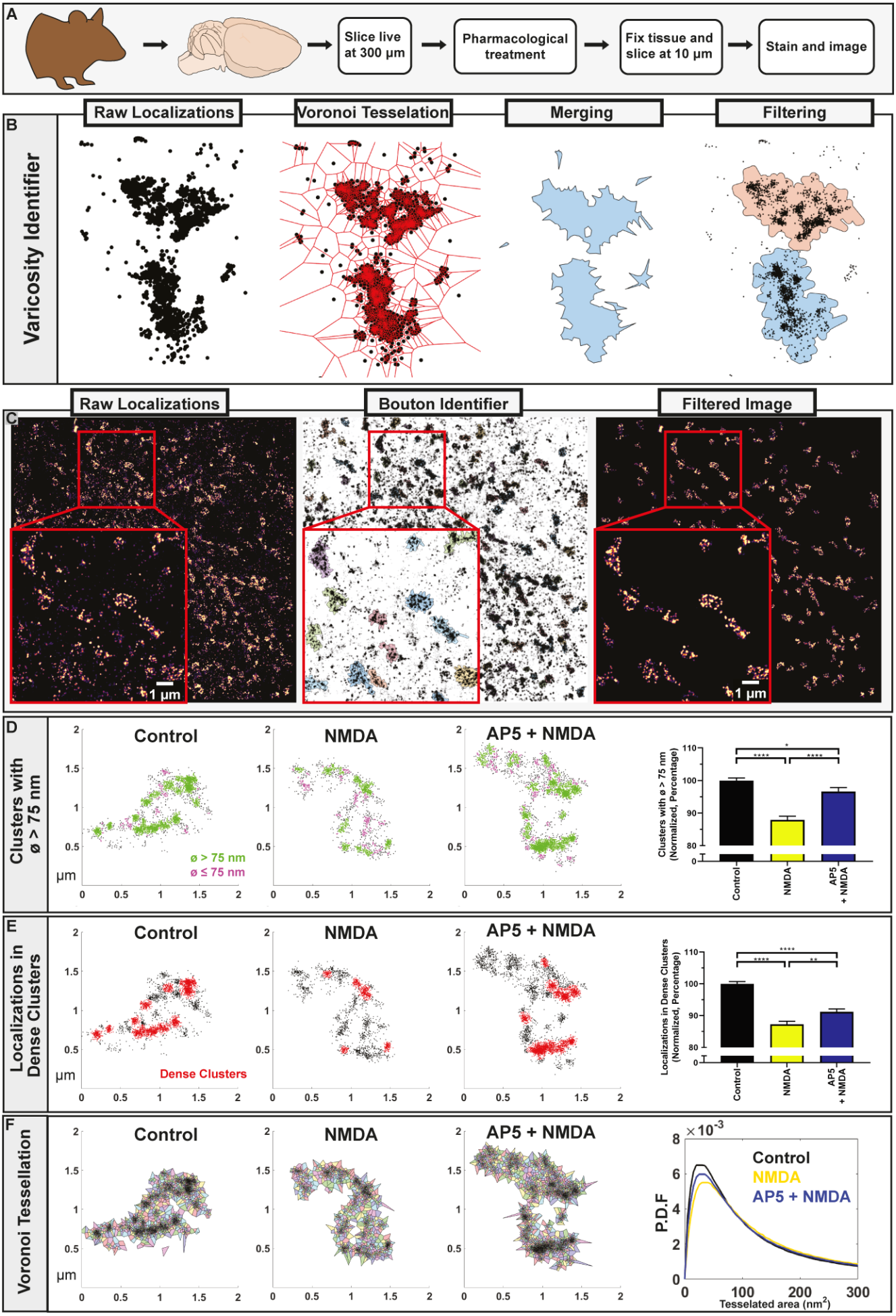
A
Slice live at 300 µm
Pharmacological treatment
Fix tissue and slice at 10 µm
Stain and image
B
Varicosity Identifier
Raw Localizations
Voronoi Tesselation
Merging
Filtering
C
Raw Localizations
Bouton Identifier
Filtered Image
1 µm
1 µm
D
Clusters with ø > 75 nm
Control
NMDA
AP5 + NMDA
ø > 75 nm
ø ≤ 75 nm
µm
Clusters with ø > 75 nm (Normalized, Percentage)
Control
NMDA
AP5 + NMDA
E
Localizations in Dense Clusters
Control
NMDA
AP5 + NMDA
Dense Clusters
µm
Localizations in Dense Clusters (Normalized, Percentage)
Control
NMDA
AP5 + NMDA
F
Voronoi Tessellation
Control
NMDA
AP5 + NMDA
µm
P.D.F
Control
NMDA
AP5 + NMDA
Tesselated area (nm²)

Figure 4

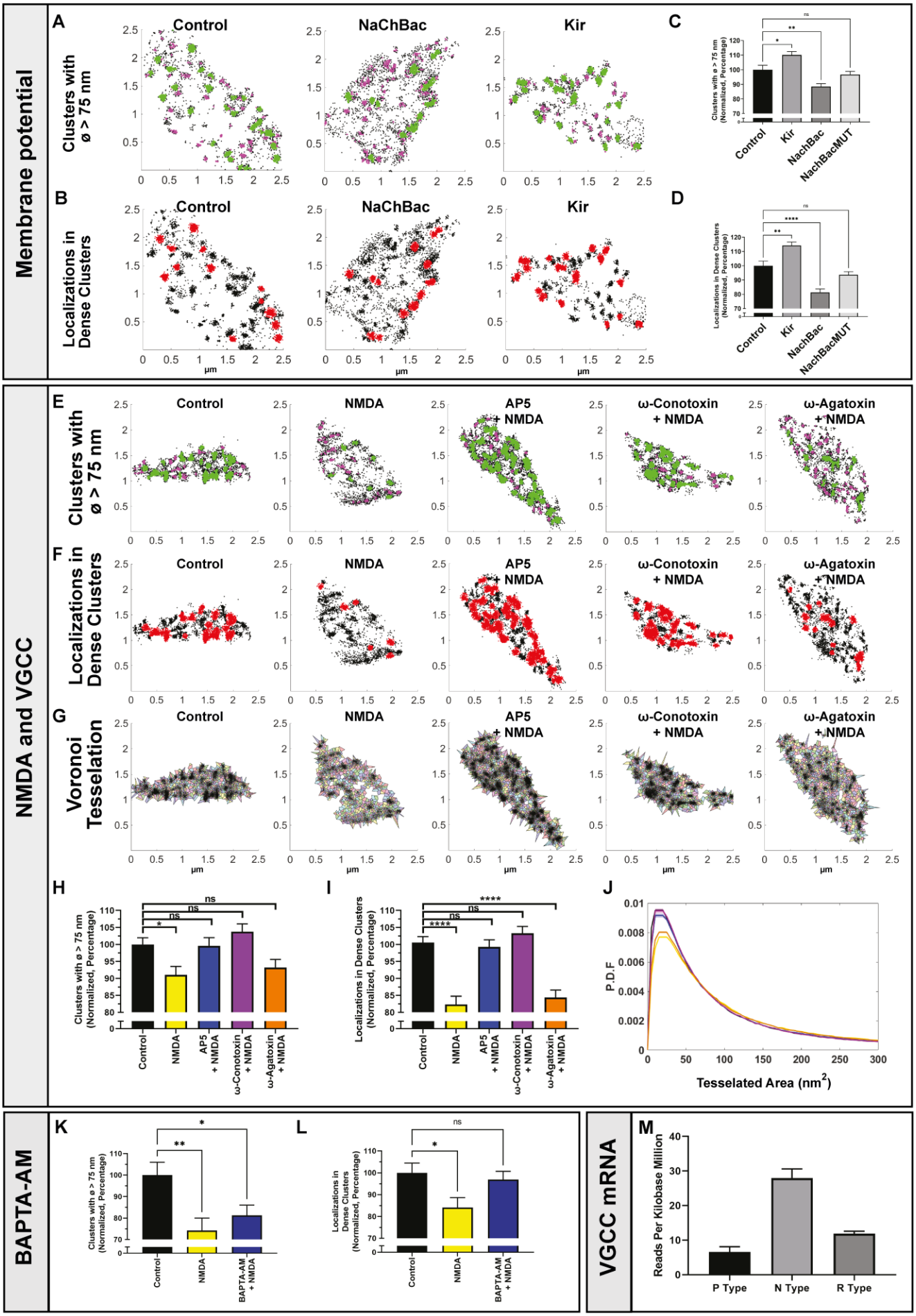
Membrane potential
A
Clusters with ø > 75 nm
Control
NaChBac
Kir
B
Localizations in Dense Clusters
µm
C
Clusters with ø > 75 nm (Normalized, Percentage)
Control
Kir
NachBac
NachBacMUT
D
Localizations in Dense Clusters (Normalized, Percentage)
NMDA and VGCC
E
Clusters with ø > 75 nm
NMDA
AP5 + NMDA
ω-Conotoxin + NMDA
ω-Agatoxin + NMDA
F
Localizations in Dense Clusters
G
Voronoi Tesselation
H
Clusters with ø > 75 nm (Normalized, Percentage)
AP5 + NMDA
ω-Conotoxin + NMDA
ω-Agatoxin + NMDA
I
Localizations in Dense Clusters (Normalized, Percentage)
J
P.D.F
Tesselated Area (nm²)
BAPTA-AM
K
Clusters with ø > 75 nm (Normalized, Percentage)
BAPTA-AM + NMDA
L
Localizations in Dense Clusters (Normalized, Percentage)
VGCC mRNA
M
Reads Per Kilobase Million
P Type
N Type
R Type

Figure 5

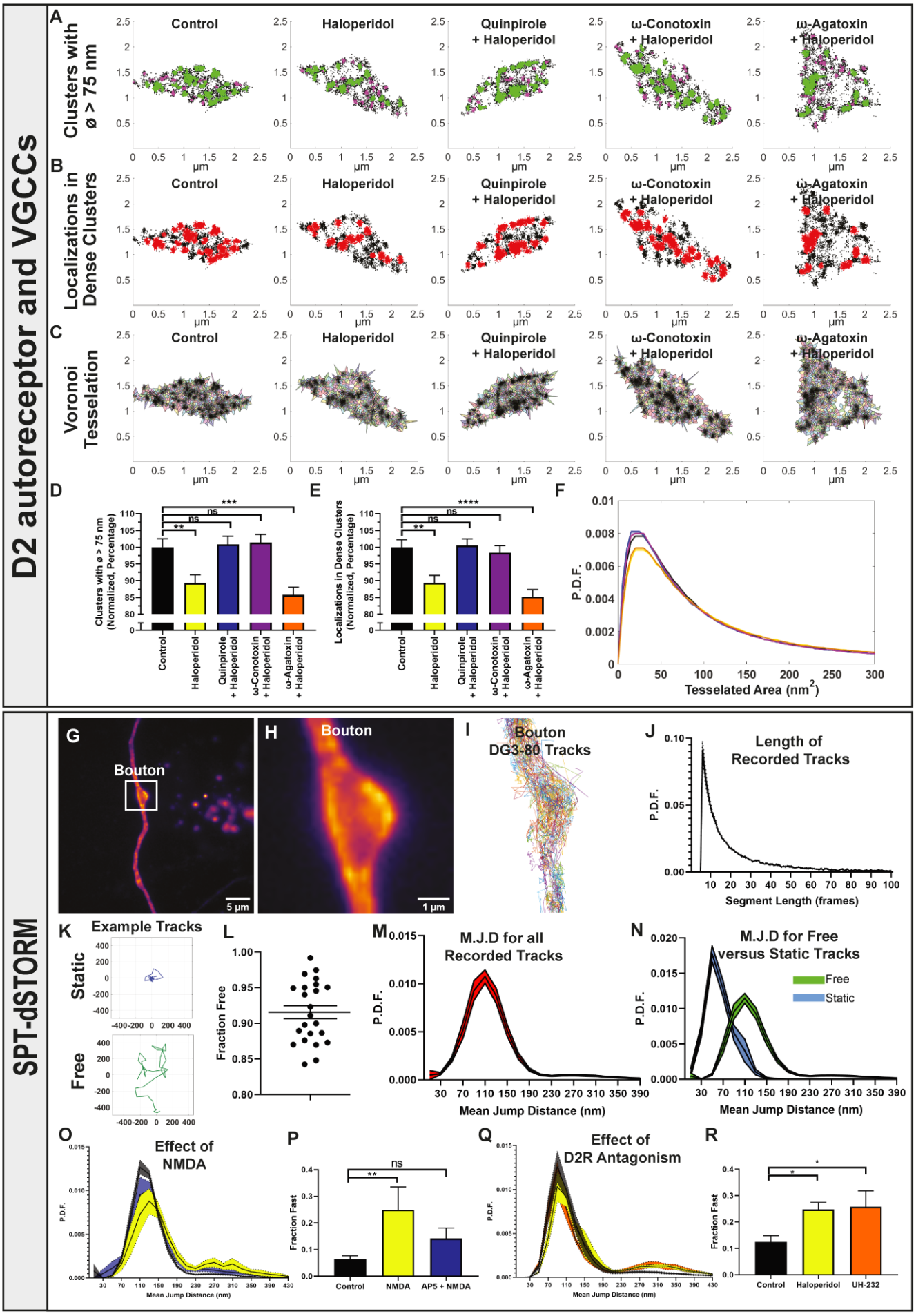
D2 autoreceptor and VGCCs
A
Clusters with ø > 75 nm
Control
Haloperidol
Quinpirole + Haloperidol
ω-Conotoxin + Haloperidol
ω-Agatoxin + Haloperidol
B
Localizations in Dense Clusters
C
Voronoi Tesselation
μm
D
Clusters with ø > 75 nm (Normalized, Percentage)
E
Localizations in Dense Clusters (Normalized, Percentage)
F
P.D.F.
Tesselated Area (nm²)
SPT-dSTORM
G
Bouton
5 μm
H
1 μm
I
Bouton DG3-80 Tracks
J
Length of Recorded Tracks
Segment Length (frames)
K
Example Tracks
Static
Free
L
Fraction Free
M
M.J.D for all Recorded Tracks
Mean Jump Distance (nm)
N
M.J.D for Free versus Static Tracks
Free
Static
O
Effect of NMDA
P
Fraction Fast
Control
NMDA
AP5 + NMDA
Q
Effect of D2R Antagonism
R
Haloperidol
UH-232

Figure 6

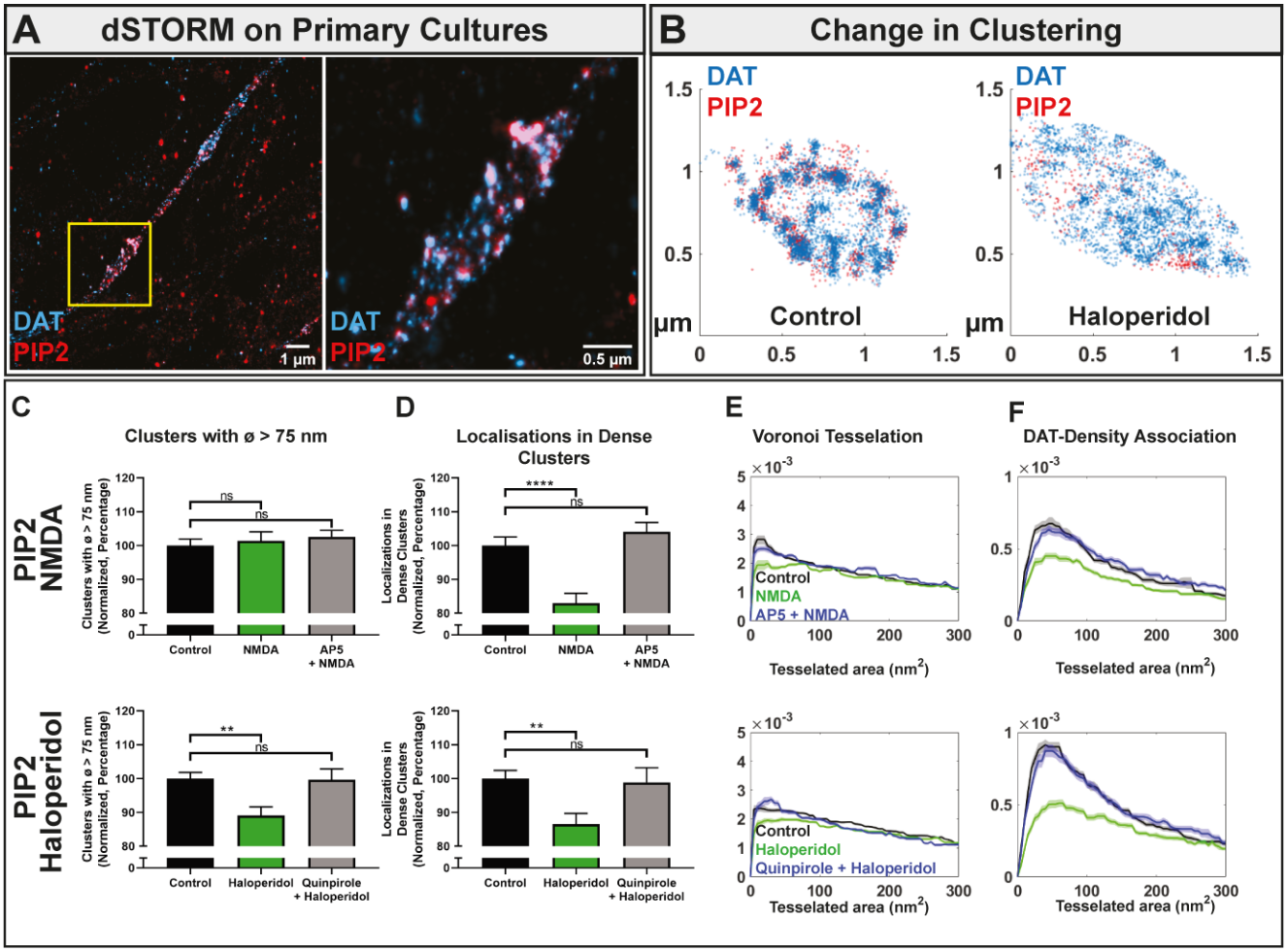
A
dSTORM on Primary Cultures
DAT
PIP2
1 µm
0.5 µm
B
Change in Clustering
DAT
PIP2
Control
Haloperidol
µm
C
Clusters with ø > 75 nm
PIP2 NMDA
PIP2 Haloperidol
Clusters with ø > 75 nm (Normalized, Percentage)
Control
NMDA
AP5 + NMDA
Haloperidol
Quinpirole + Haloperidol
ns
**
D
Localisations in Dense Clusters
Localizations in Dense Clusters (Normalized, Percentage)
****
E
Voronoi Tesselation
Tesselated area (nm²)
F
DAT-Density Association

Figure 7

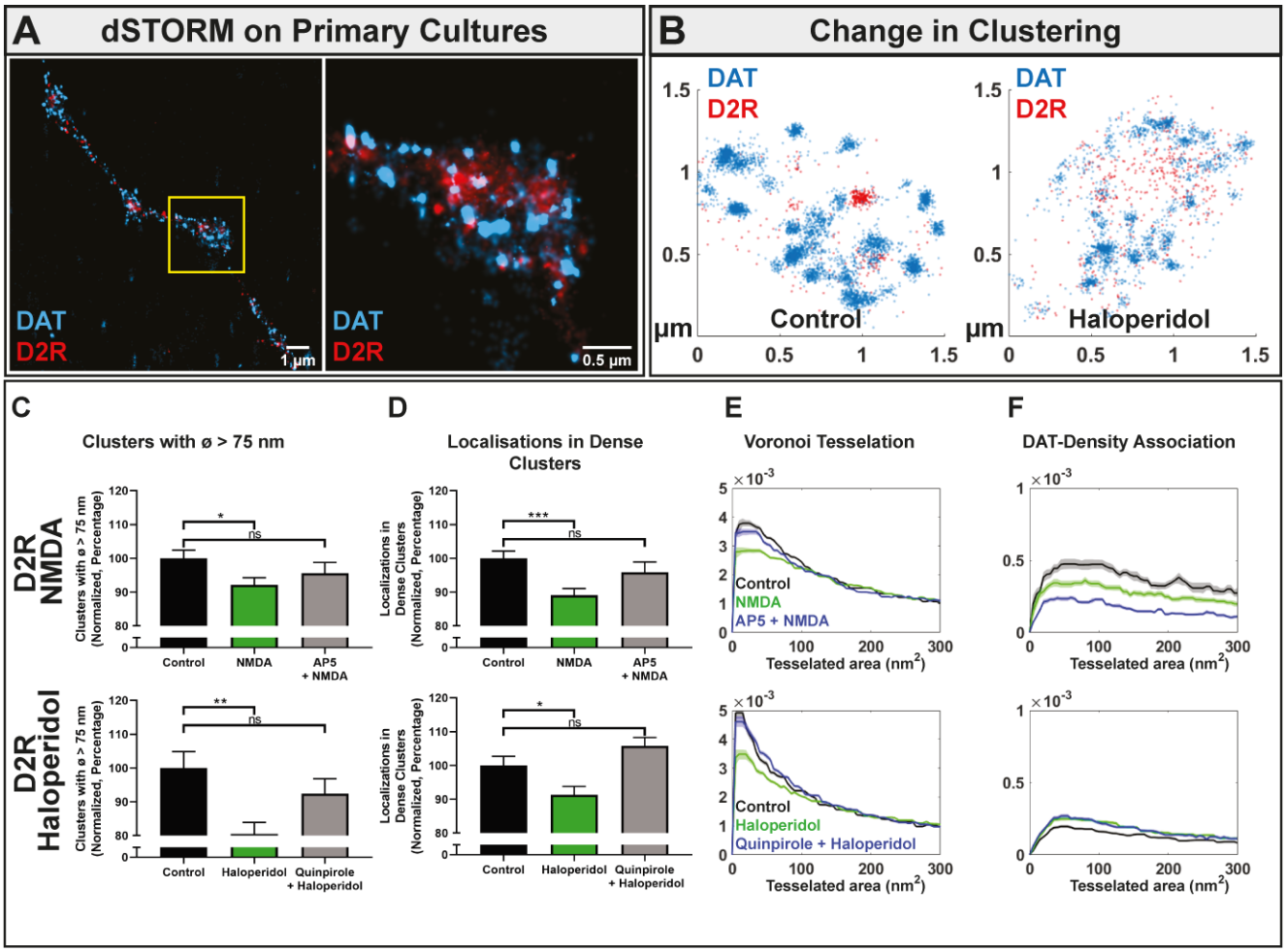
A
dSTORM on Primary Cultures
DAT
D2R
1 µm
DAT
D2R
0.5 µm
B
Change in Clustering
DAT
D2R
Control
Haloperidol
µm
C
Clusters with ø > 75 nm
D2R NMDA
D2R Haloperidol
Clusters with ø > 75 nm (Normalized, Percentage)
Control
NMDA
AP5 + NMDA
Haloperidol
Quinpirole + Haloperidol
D
Localisations in Dense Clusters
Localizations in Dense Clusters (Normalized, Percentage)
E
Voronoi Tesselation
Control
NMDA
AP5 + NMDA
Haloperidol
Quinpirole + Haloperidol
Tesselated area (nm²)
F
DAT-Density Association
Tesselated area (nm²)

Supplemental Figure S1

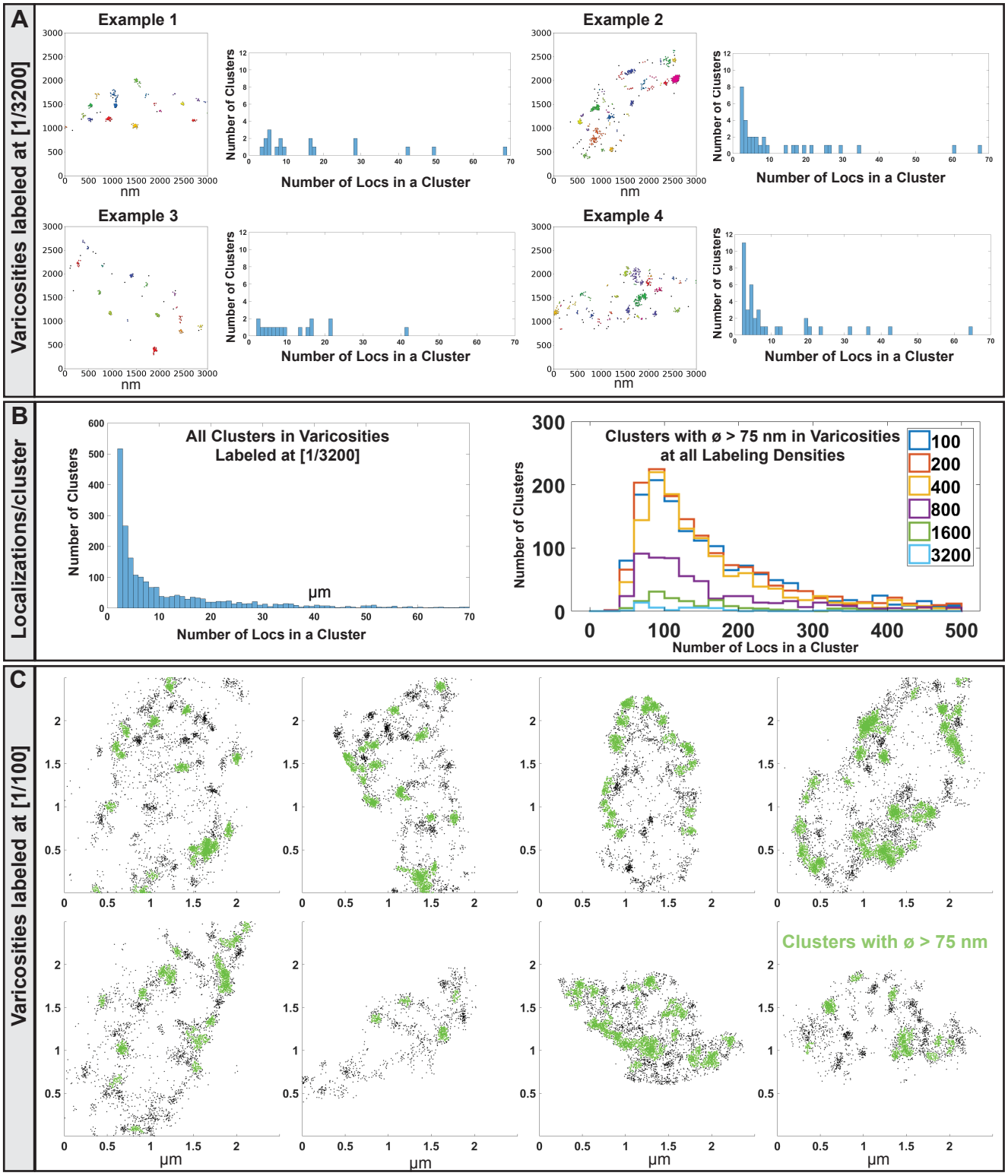

Supplemental Figure S2

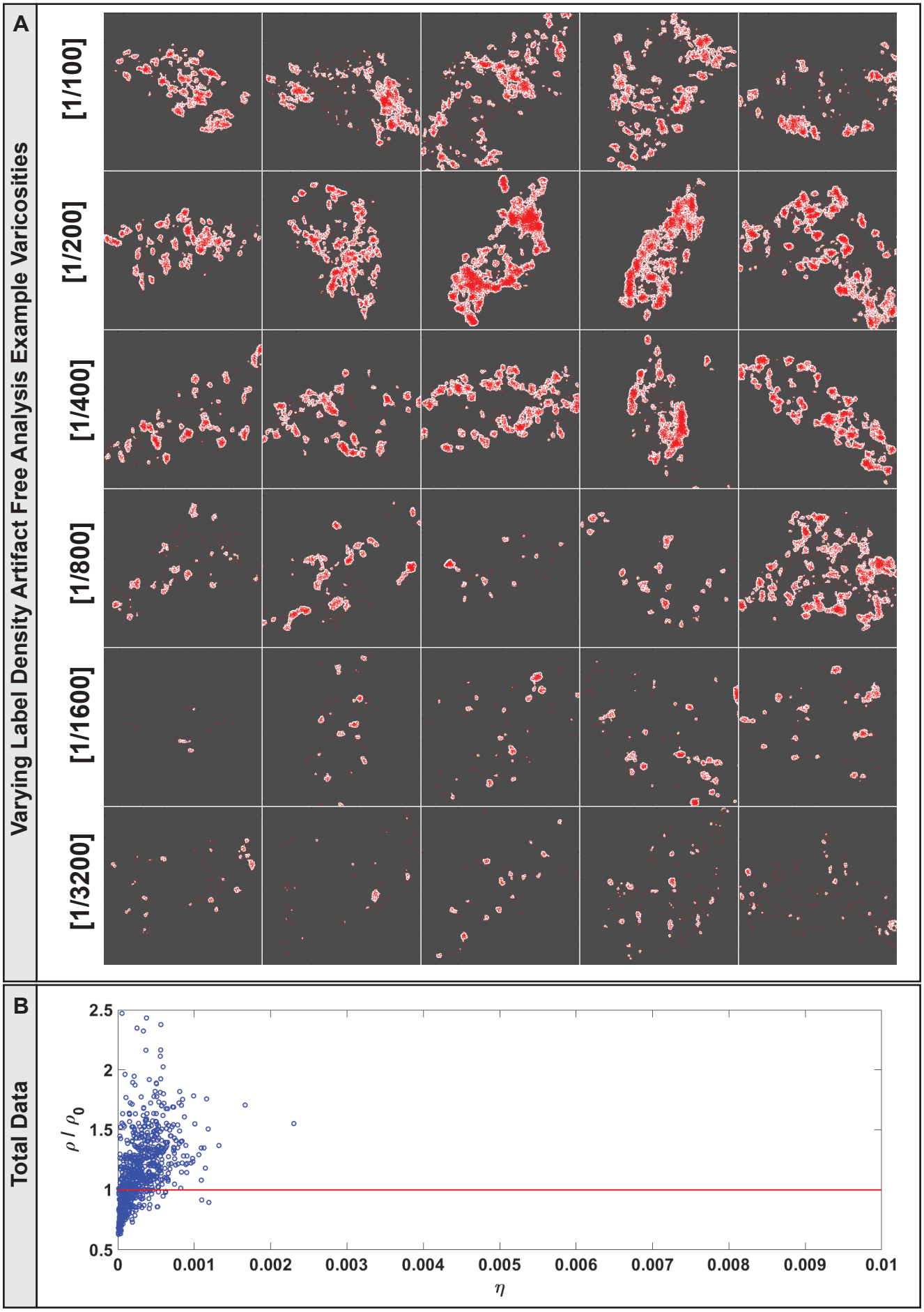

Supplemental Figure S3

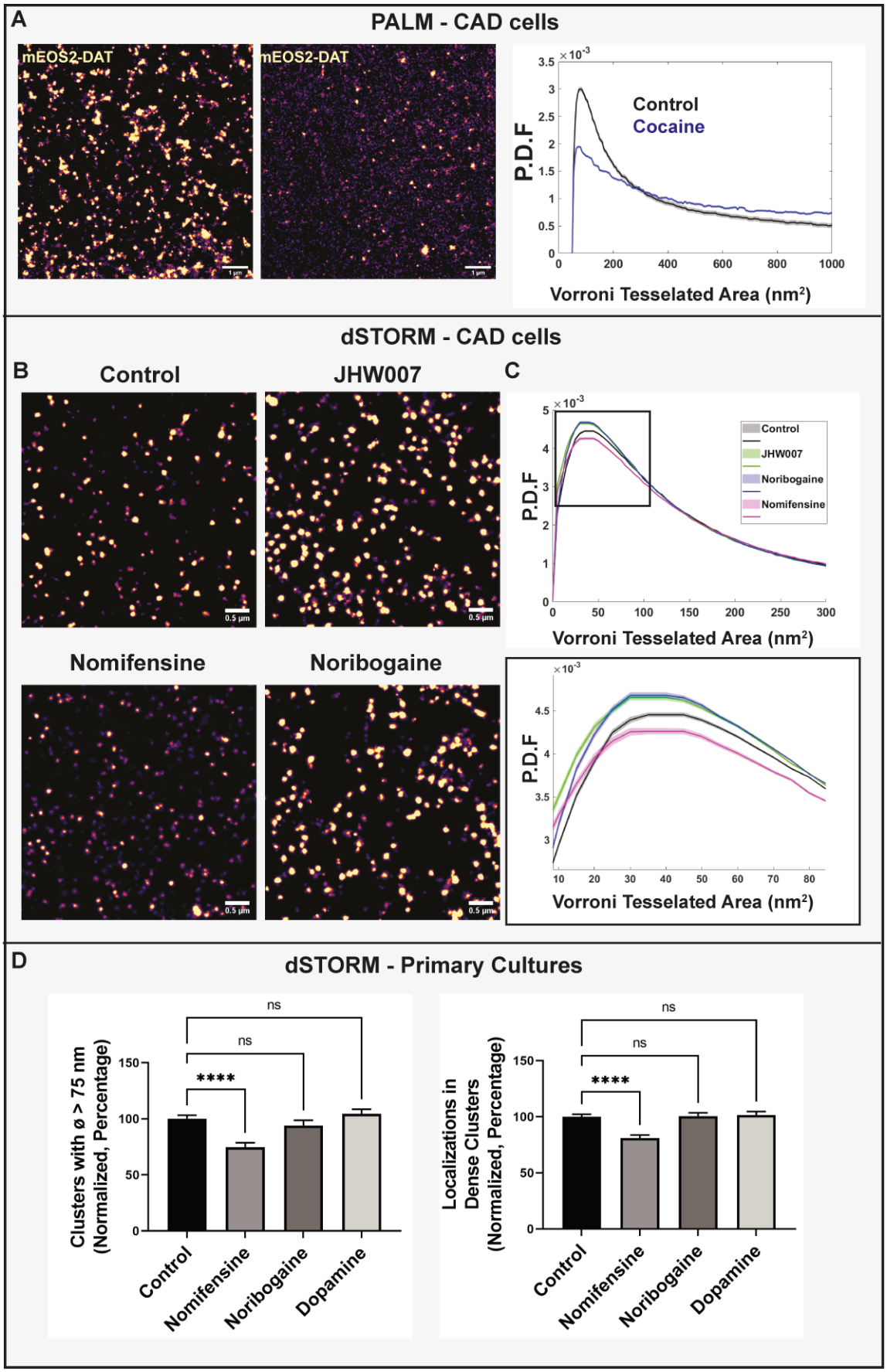

Supplemental Figure S4

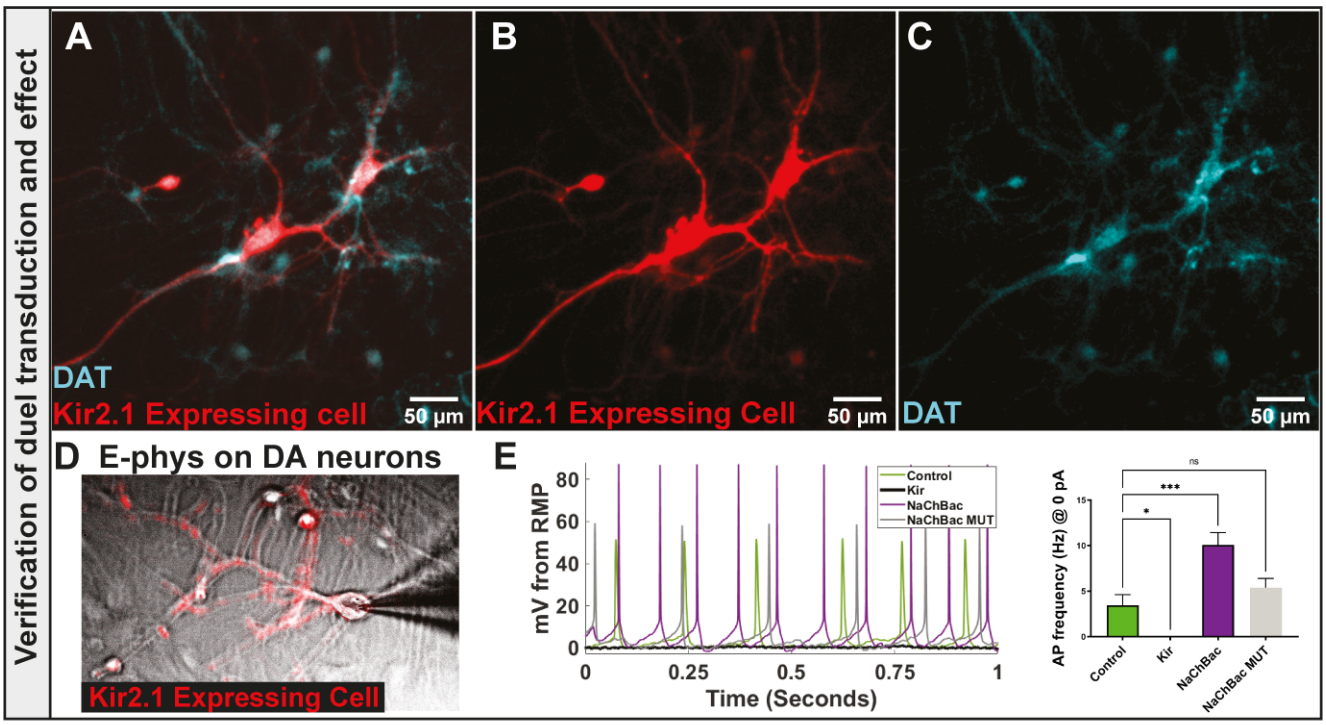

Supplemental Figure S5

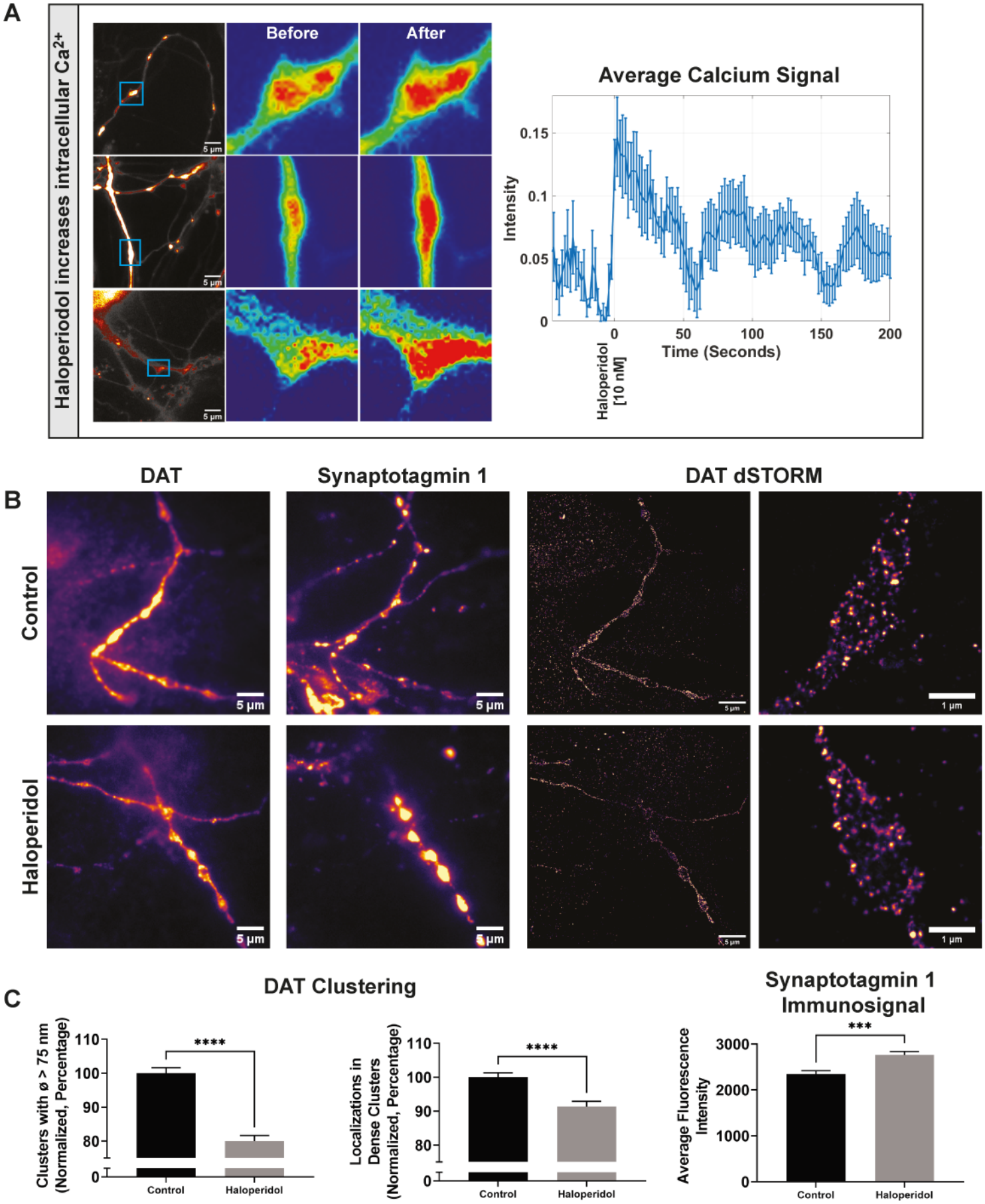

Supplemental Figure S6

Verification of D2R Antibody

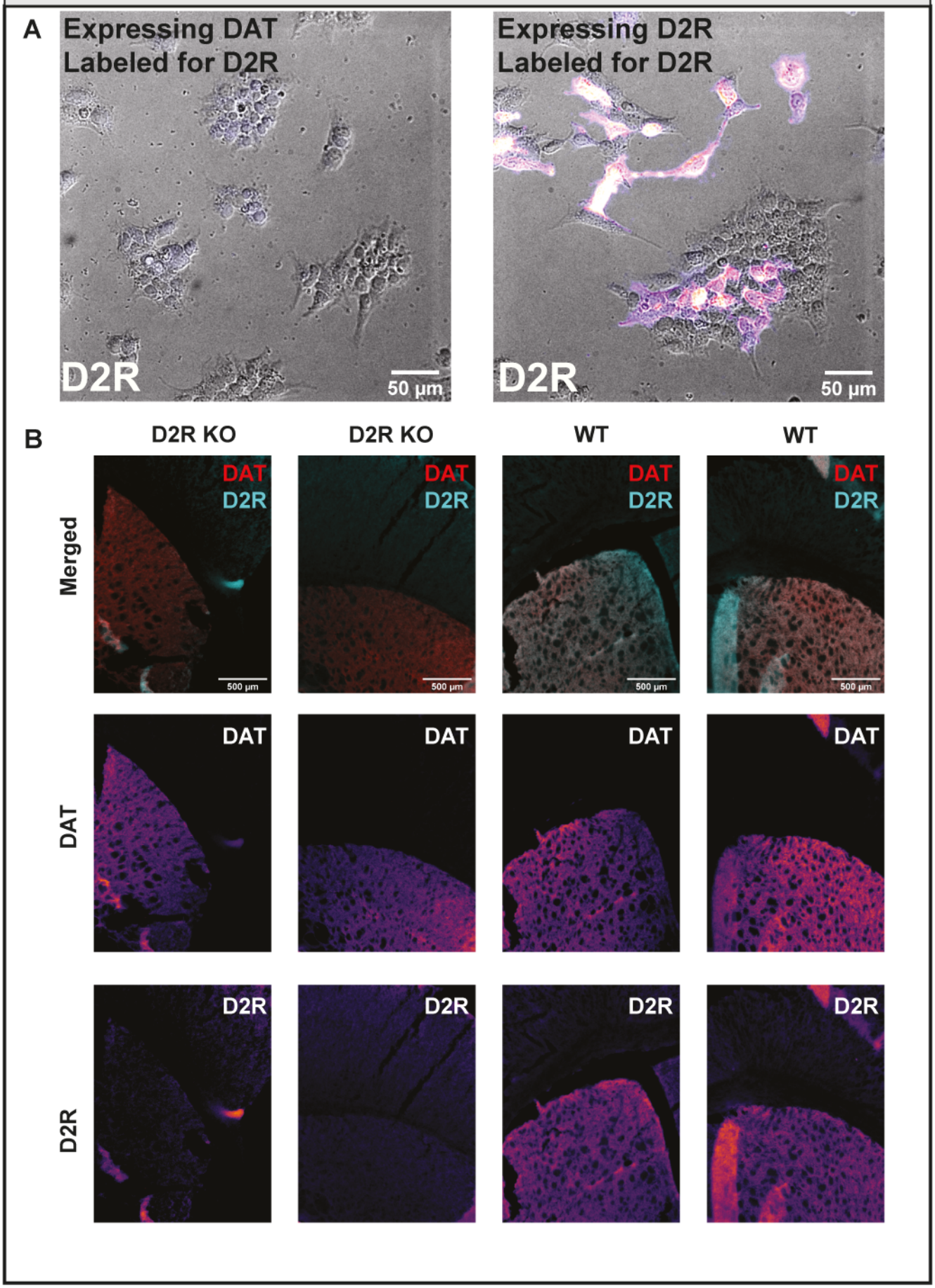

Supplemental Figure S7

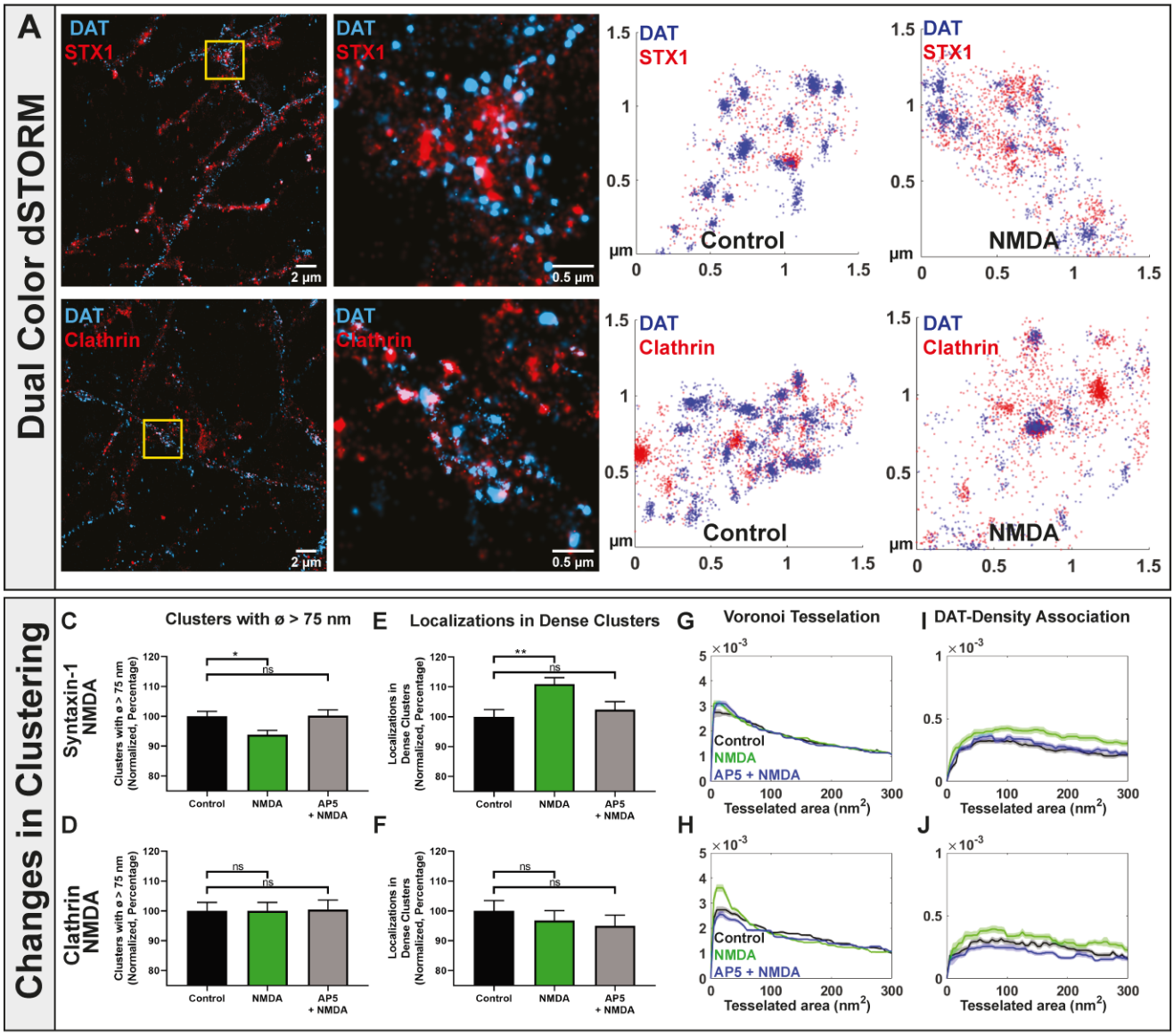
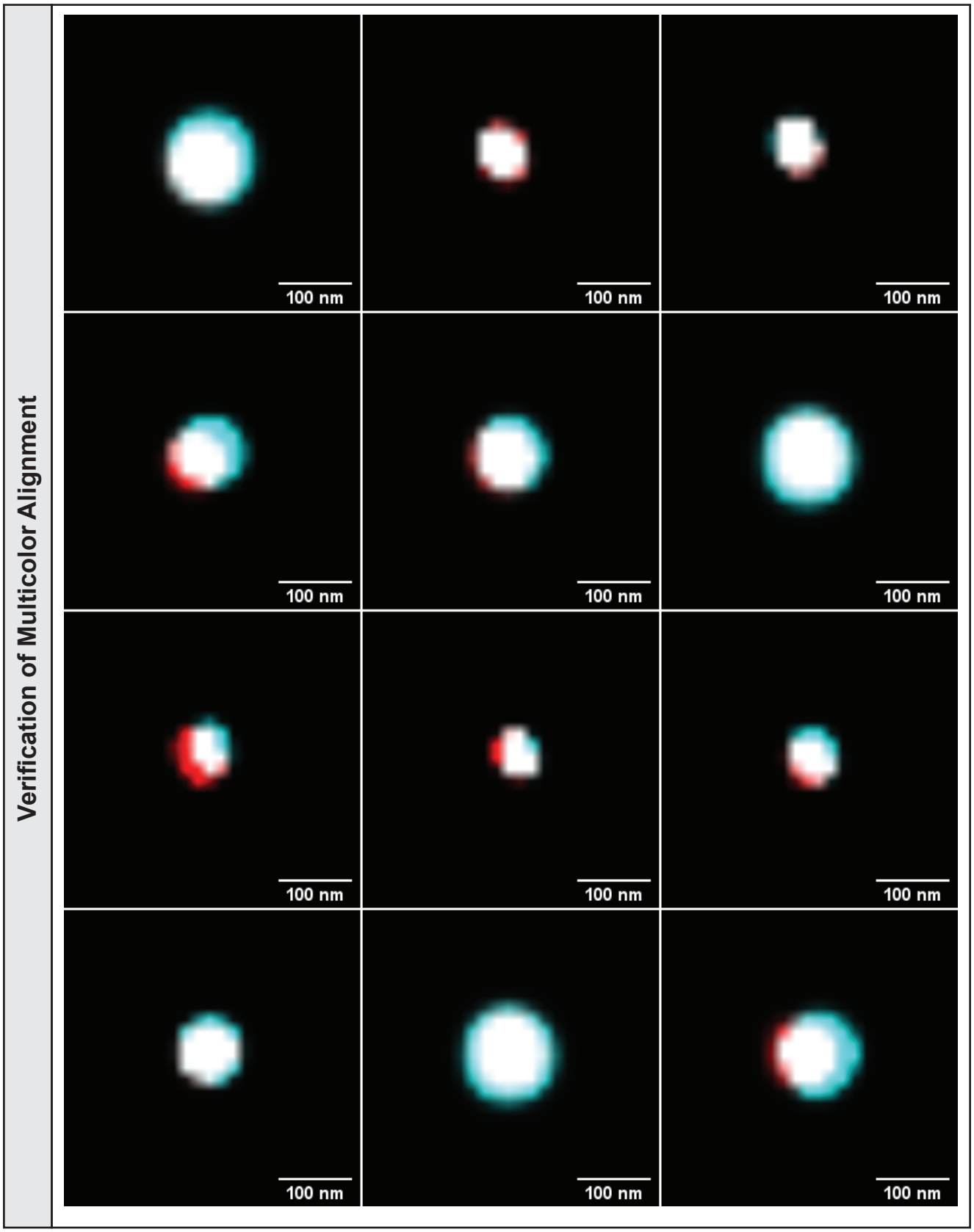
Supplemental Figure S8